1 **Large-scale genetic association and single cell accessible chromatin**

2 **mapping defines cell type-specific mechanisms of type 1 diabetes risk**

3

4 Joshua Chiou[1,#], Ryan J Geusz[1], Mei-Lin Okino[2], Jee Yun Han[3], Michael Miller[3], Paola

5 Benaglio[2], Serina Huang[2], Katha Korgaonkar[2], Sandra Heller[4], Alexander Kleger[4], Sebastian

6 Preissl[3], David U Gorkin[3], Maike Sander[2,5,6], Kyle J Gaulton[2,6,#]

7 1. Biomedical Sciences Graduate Program, University of California San Diego, La Jolla CA

8   92093

9 2. Department of Pediatrics, Pediatric Diabetes Research Center, University of California San

10   Diego, La Jolla CA 92093

11 3. Center for Epigenomics, Department of Cellular and Molecular Medicine, University of

12   California San Diego, La Jolla CA 92093

13 4. Department of Internal Medicine I, Ulm University, Ulm, Germany

14 5. Department of Cellular and Molecular Medicine, University of California San Diego, La Jolla

15   CA 92093

16 6. Institute for Genomic Medicine, University of California San Diego, La Jolla CA 92093

17

18 # Corresponding authors:

19 Kyle J Gaulton

20 9500 Gilman Drive, #0746

21 Department of Pediatrics

22 University of California San Diego

23 858-822-3640

24 kgaulton@ucsd.edu

25

26 Joshua Chiou

27 9500 Gilman Drive, #0746

28 Biomedical Sciences Graduate Program

29 University of California San Diego

30 510-449-8870

31 joshchiou@ucsd.edu

32 **ABSTRACT**

33 Translating genome-wide association studies (GWAS) of complex disease into mechanistic

34 insight requires a comprehensive understanding of risk variant effects on disease-relevant cell

35 types. To uncover cell type-specific mechanisms of type 1 diabetes (T1D) risk, we combined

36 genetic association mapping and single cell epigenomics. We performed the largest to-date

37 GWAS of T1D in 489,679 samples imputed into 59.2M variants, which identified 74 novel

38 association signals including several large-effect rare variants. Fine-mapping of 141 total signals

39 substantially improved resolution of causal variant credible sets, which primarily mapped to non-

40 coding sequence. To annotate cell type-specific regulatory mechanisms of T1D risk variants, we

41 mapped 448,142 candidate *cis*-regulatory elements (cCREs) in pancreas and peripheral blood

42 mononuclear cell types using snATAC-seq of 131,554 nuclei. T1D risk variants were enriched in

43 cCREs active in CD4+ T cells as well as several additional cell types including pancreatic exocrine

44 acinar and ductal cells. High-probability T1D risk variants at multiple signals mapped to exocrine-

45 specific cCREs including novel loci near *CEL, GP2* and *CFTR*. At the *CFTR* locus, the likely

46 causal variant rs7795896 mapped in a ductal-specific distal cCRE which regulated *CFTR* and the

47 risk allele reduced transcription factor binding, enhancer activity and *CFTR* expression in ductal

48 cells. These findings support a role for the exocrine pancreas in T1D pathogenesis and highlight

49 the power of combining large-scale GWAS and single cell epigenomics to provide insight into the

50 cellular origins of complex disease.

INTRODUCTION

Type 1 diabetes (T1D) is a complex autoimmune disease characterized by the loss of insulin-producing pancreatic beta cells and subsequent hyperglycemia[1], where the triggers of autoimmunity and disease onset remain poorly understood. T1D has a strong genetic component, most prominently at the major histocompatibility complex (MHC) locus but including 60 additional risk loci identified in genome-wide and targeted array association studies[2–6]. T1D associated variants at risk loci are largely non-coding, and intersection of T1D associated variants with epigenomic data has identified an enrichment of risk variants within lymphoid enhancers[2]. However, due to limited sample sizes, incomplete variant coverage, and the limited cell type resolution of existing epigenomic maps, the causal variants and cellular mechanisms of action of T1D risk loci are largely unresolved.

RESULTS

Comprehensive discovery and fine mapping of T1D risk signals

To discover novel risk loci and improve fine mapping of causal variants for T1D, we performed a genome-wide association study (GWAS) of 18,803 T1D cases and 470,876 controls of European ancestry from 9 country-of-origin and array-matched cohorts (**Supplemental Table 1**). After applying uniform quality-control measures (**Supplemental Figure 1**), where we removed low-quality genotypes, individuals of non-European ancestry, or controls with other autoimmune diseases, we imputed genotypes into the TOPMed r2 panel and tested for T1D association[7]. Through meta-analysis, we combined association results for 59,244,856 variants across cohorts and observed 80 loci reaching genome-wide significance ($P<5\times10^{-8}$), including 30 loci previously unreported in T1D risk (**Figure 1a**, **Supplemental Figure 2, Supplemental Table 2**). Previous studies have identified independent association signals at multiple T1D loci[2], and we reasoned that our increased sample size would uncover additional independent signals. Through iterative conditional analyses, we discovered 52 secondary signals at locus-wide significance ($P<1\times10^{-5}$), of which 44 were previously unknown (**Supplemental Figure 3, Supplemental Table 2**). Over 40% (36/89) of loci contained more than one independent signal; for example, the known *BACH2* locus and novel *BCL11A* locus each had three signals (**Figure 1b**), and at the *IL2RA* locus we identified six independent signals, three of which were novel (**Supplemental Figure 3**).

The TOPMed r2 panel enables more accurate imputation of rare variants over previous reference panels, and in our study, we identified five novel T1D-associated variants with minor allele

83   frequency (MAF) less than 0.005 and large effects on disease risk (**Supplemental Table 2,**

84   **Supplemental Figure 4**). Among these rare variants, rs541856133 (MAF=.0015, OR=2.97)

85   mapped to a non-coding region directly upstream of *CEL,* which has been implicated previously

86   as the cause of maturity-onset diabetes of the young with pancreatic exocrine dysfunction

87   (MODY8)[8]. We also identified a novel protein-coding protective variant at *IFIH1* (p.Asn160Asp,

88   rs75671397, MAF=.002, OR=0.32), which was conditionally independent of the known protein-

89   coding variant signals in this gene. The three additional rare T1D risk variants mapped to non-

90   coding regions at the 16q23 (rs138099003, MAF=.0015, OR=2.29), *SH2B3* (rs762349492,

91   MAF=.0018, OR=1.99), and *TOX* (rs192456638, MAF=.0045, OR=1.80) loci (**Supplemental**

92   **Table 2, Supplemental Figure 4**).

93   We next sought to fine map causal variants of T1D signals using a Bayesian approach[9]. In total

94   we considered 141 signals including 89 primary and 52 conditional signals at known and novel

95   loci excluding the MHC locus due to complex LD structure (**Figure 1c**). We defined linkage

96   disequilibrium (LD)-based credible sets for the 141 signals, using new index variants at known

97   loci where applicable. For each signal, we then used approximate Bayes factors[9] to calculate the

98   posterior probability of association (PPA) for each variant and defined credible sets of variants

99   that summed up to 99% cumulative PPA (**Supplemental Table 3**). Compared to previous

100   efforts[2,10], our fine-mapping resolution was drastically improved based on two complementary

101   measures: 1) fewer number of credible set variants per signal (median 24 variants) and 2) a

102   greater number of variants with high causal probabilities (**Figure 1d**). At nearly half of all T1D

103   signals (49%; 69/141) the credible set contained 20 or fewer variants, and 25% (35/141)

104   contained a single variant explaining the majority of the posterior probability (>50% PPA). Among

105   credible set variants, 23 variants with PPA>1% were nonsynonymous changes, including several

106   at novel loci p.Arg471Cys in *AIRE* (PPA=.99), p.Val11Ile in *BATF3* (PPA=.081), p.Ala91Val in

107   *PRF1* (PPA=0.038), and p.Val131Phe in *CD3G* (PPA=.028) (**Supplemental Table 4**).

108   Given our comprehensive genome-wide T1D genetic association and fine-mapping data, we used

109   these data to derive insight into disease pathophysiology. We therefore broadly characterized

110   relationships between T1D and other complex traits and diseases by performing genome-wide

111   genetic correlation analyses using LD score regression. As expected, T1D had significant

112   (FDR<.10) positive correlations with autoimmune diseases including rheumatoid arthritis (r_g=0.43,

113   FDR=7.34×10^{-5}), systemic lupus erythematosus (r_g=0.36, FDR=2.52×10^{-7}), celiac disease

114   (r_g=0.28, FDR=1.11×10^{-3}), and autoimmune vitiligo (r_g=0.30, FDR=2.02×10^{-5}), as well as a

115   negative correlation with ulcerative colitis (r_g=-0.17, FDR=2.94×10^{-3}) (**Supplemental Figure 5**).

116 Among other traits, we observed significant positive correlations with metabolic traits and

117 diseases such as fasting proinsulin (r_g=0.18, FDR=8.91×10^{-2}) and fasting insulin level, (r_g=0.18,

118 FDR=6.85×10^{-3}), coronary artery disease (r_g=0.12, FDR=6.85×10^{-3}) and type 2 diabetes (r_g=0.10,

119 FDR=4.39×10^{-3}), and positive correlations with pancreatic diseases such as pancreatic cancer

120 (r_g=0.25, FDR=7.40×10^{-2}) and chronic pancreatitis (r_g=0.13, FDR=3.84×10^{-1}), although the latter

121 estimate was not significant. These results demonstrate relationships between genetic effects on

122 T1D risk and a diversity of traits including autoimmune, pancreatic and metabolic disease.

123 **Defining cell type-specific *cis*-regulatory programs in T1D-relevant tissues**

124 The large majority of T1D risk signals map to non-coding regions and likely affect gene

125 regulation[2]. In order to annotate gene regulatory programs affected by T1D risk variants, we

126 generated a reference map of cell type-specific accessible chromatin using single nucleus ATAC-

127 seq (snATAC-seq) assays of T1D-relevant tissues including peripheral mononuclear blood cells

128 (PBMC), purified pancreatic islets, and whole pancreas tissue from non-diabetic donors

129 (**Supplemental Table 5**). To cluster cells obtained from these assays, we used a modified version

130 of our previous pipeline[11] that included rigorous quality control, removal of potential doublets, and

131 removal of potential confounding effects between different donors, tissues, and technologies to

132 group 131,554 chromatin accessibility profiles into 28 clusters (**Figure 2a, Supplemental Figure**

133 **6**). We assigned cell type identity to each cluster using the chromatin accessibility profiles of gene

134 bodies for known marker genes, and identified cells representing lymphoid, myeloid, endocrine,

135 exocrine, endothelial, and stellate cell types (**Figure 2a-b**). Within lymphoid and myeloid cells,

136 there were clusters representing both peripheral blood cells as well as tissue resident cells in the

137 pancreas based on both marker gene accessibility and tissue-of-origin profiles (**Figure 2a-b,**

138 **Supplemental Figure 6**). For example, we observed accessibility at *C1QB* marking pancreatic

139 tissue-resident macrophages, at *REG1A* marking pancreatic acinar cells, and at *CFTR* marking

140 pancreatic ductal cells (**Figure 2b**). We also observed distinct patterns of chromatin accessibility

141 at marker genes between different clusters of the same cell type allowing us to further discriminate

142 specific sub-types such as *FOXP3* for regulatory T cells relative to other T cells and *TCL1A* for

143 naïve B cells relative to memory B cells (**Figure 2b**).

144 To characterize the regulatory programs of each cell type and cell state, we aggregated reads

145 from cells within each cluster and called accessible chromatin sites representing candidate *cis*-

146 regulatory elements (cCREs). Across all 28 clusters, we identified a total of 448,142 cCREs and

147 an average of 77,812 cCREs per cluster (**Supplementary Data 1**). To further define regulatory

148 programs defining the identity of each cell type, we calculated the relative accessibility of each

149   cCRE across all clusters and identified 25,436 cell type-specific cCREs with accessibility patterns

150   specific to a given cluster (**Figure 2c, Supplementary Data 2**). To confirm that cell type-specific

151   cCREs regulated key processes involved in cellular identity, we identified gene ontology (GO)

152   terms enriched for each set of cell type-specific cCREs using GREAT[12]. GO terms significantly

153   enriched in cell type-specific cCREs represented highly specialized cellular processes, for

154   example inflammatory response for pancreatic tissue-resident macrophages ($P=6.09\times10^{-12}$),

155   extracellular matrix organization for activated stellate cells ($P=1.47\times10^{-41}$), transepithelial water

156   transport for ductal cells ($P=1.26\times10^{-21}$) and digestion for acinar cells ($P=1.18\times10^{-11}$) (**Figure 2c,**

157   **Supplementary Table 6**).

158   We next decoded the regulatory logic underlying cCRE activity for each cell type. First, we

159   identified candidate transcription factors (TFs) regulating cCRE activity by identifying sequence

160   motifs enriched in accessible chromatin of each cell type using chromVAR[13]. There were 290

161   motifs in JASPAR[14] with evidence for variable enrichment across cell types (**Supplementary**

162   **Table 7**). Enriched motifs included TF families with lineage-specific enrichment such as SPI in

163   myeloid and B cells, ETS in T cells, and FOXA in pancreatic endocrine and exocrine cells[15–17]

164   (**Figure 2d**). We also identified motifs enriched in specific cell types such as NR5A in acinar

165   cells[18], HNF1 in ductal cells[19], and EBF in B cells[20] (**Figure 2d**), as well as motifs for TF families

166   enriched in specific states within a cell type, such as POU2 in memory B cells[21], TCF7 in naïve

167   CD4+ T cells[22], and RUNX in adaptive NK cells[23] (**Figure 2d**). Second, we defined cell type-

168   resolved links between distal cCREs and putative target gene promoters using co-accessibility

169   across single cells with Cicero[24]. Considering all cell types, we observed a total of 1,028,428 links

170   between distal cCREs and gene promoters (**Supplemental Data 3**), where 145,138 distinct distal

171   cCREs were linked to at least one promoter. In many cases, co-accessible links were highly cell

172   type-specific; for example, multiple distal cCREs were co-accessible with the *AQP1* promoter in

173   ductal cells and the *CEL* promoter in acinar cells, none of which were identified in other cell types

174   (**Figure 2e**). Together these results identify candidate transcriptional regulators and target genes

175   of distal cCREs in pancreatic and immune cell types.

176   **Annotating fine-mapped T1D risk variants with cell type-specific regulatory programs**

177   We reasoned that our cell type-resolved regulatory maps would enable deeper insight into

178   pancreatic and blood cell types involved in T1D pathogenesis. We therefore determined

179   enrichment of variants associated with T1D as well as other complex diseases[25–42] and qualitative

180   endophenotypes[43–52] for cCREs using stratified LD score regression[53]. For T1D, the most

181   significant enrichment was for variants in CD4+ T cell cCREs (naïve CD4+ T Z=4.54,

182 FDR=$1.26×10^{-3}$; activated CD4+ T Z=3.83, FDR=$5.88×10^{-3}$; regulatory T Z=3.26, FDR=$1.35×10^{-2}$) (**Figure 3a**). Notably, we did not observe evidence for enrichment in resident immune cells in the pancreas (pancreatic CD8+ T cell Z=0.46, FDR=0.93; pancreatic tissue-resident macrophage Z=-1.02, FDR=1.0). Outside of immune cell types, pancreatic ductal cell cCREs had the strongest T1D enrichment, although this estimate was not significant (ductal Z=0.46, FDR=0.93). Other immune-related diseases were also enriched within lymphocyte cCREs, although Crohn's disease was also enriched for monocytes and conventional dendritic cell cCREs (**Figure 3a**). As expected, type 2 diabetes and glycemic traits were strongly enriched in pancreatic endocrine cell cCREs, but interestingly, glycemic traits such as glucose levels at 2 hours post-OGTT were also enriched in pancreatic acinar and ductal cell cCREs (**Figure 3a**). Together these results demonstrate that T1D associated variants are broadly enriched for CD4+ T cell cCREs, and highlight other complex traits and diseases enriched for pancreatic and immune cell type cCREs.

194 Despite the strong enrichment of T1D-associated variants in CD4+ T cells, less than half of fine-mapped T1D signals overlapped a CD4+ T cell cRE, suggesting that additional cell types contribute to T1D risk. In order to identify additional disease-relevant cell types, we used an orthogonal approach to test for enrichment of T1D variants within the subset of cCREs specific to each cell type (from **Figure 2c; see Methods**). As expected, T1D variants genome-wide were enriched in cCREs specific to CD4+ T cells (activated CD4+ T log enrich=4.14, 95% CI=0.97-5.37) as well as pancreatic beta cells (log enrich=3.64, 95% CI=1.23-4.90) (**Figure 3b**). Interestingly, T1D variants were also enriched in cCREs specific to plasmacytoid dendritic cells (log enrich=4.08, 95% CI=2.09-5.16), classical monocytes (log enrich=4.04, 95% CI=2.74-4.92), and pancreatic acinar and ductal cells (ductal log enrich=3.43, 95% CI=1.07-4.71, acinar log enrich=2.74, 95% CI=0.66-4.02) (**Figure 3b**). We further enumerated the contribution of these cell types to T1D risk by determining the cumulative posterior probability (cPPA) of fine-mapped variants overlapping cell type-specific cCREs after removing variants overlapping a more probable cell type (**see Methods**). Among broad annotation categories, distal cCREs harbored the most cumulative risk (cPPA=24.3, N_{vars}=291), followed by coding exons (cPPA=7.98, N=34) and promoters (cPPA=6.63, N=55) (**Figure 3c**). When breaking down distal cCREs by cell type categories, CD4+ T cells had the most cumulative risk (cPPA=9.7, N=112), followed by exocrine cells (acinar and ductal; cPPA=6.2, N=51), monocytes (cPPA=3.1, N=54), and then endocrine cells (cPPA=2.3, N=33) (**Figure 3c**).

213 Given insight into cell types contributing to T1D risk, we next annotated individual T1D signals in cCREs for these cell types. Over 75% (109/141) of T1D signals contained at least one fine-

215   mapped variant (with PPA>.01) overlapping a cCRE, and at 83% (90/109) of these signals the

216   cCRE was further co-accessible with at least one gene promoter (**Supplementary Table 8**). For

217   each T1D signal, we calculated the cPPA of fine-mapped variants overlapping cCREs for disease-

218   enriched cell types. At 58 T1D signals a fine-mapped variant overlapped a CD4+ T cell cCRE,

219   and signals with the highest cPPA in CD4+ T cells included the *CD2, IL2RA, PRF1* and *IKZF4*

220   loci (**Figure 3d**). We also identified T1D signals with high cPPA in pancreatic acinar and ductal

221   (exocrine) cCREs and monocyte cCREs, many of which were cell type-specific (**Figure 3d**). For

222   example, three variants at the *GP2* locus accounted for .951 of the PPA and mapped in an acinar-

223   specific cCRE co-accessible with the promoter of *GP2*, which encodes the major membrane

224   glycoprotein of pancreatic zymogen granules (**Figure 3e**). Similarly, rs72802342 at the *BCAR1*

225   locus (PPA=.30) mapped in an acinar-specific cCRE co-accessible with the *CTRB1* and *CTRB2*

226   promoters (**Figure 3f**). We observed similar predicted mechanisms in acinar cells at the *RNLS*

227   and *COBL* loci, as well as the novel *CEL* locus, where rs541856133 (PPA=.99) mapped in a

228   region of broad acinar-specific accessibility although not in a cCRE directly (**Supplementary**

229   **Figure 7a-c**). At *CTLA4*, variant rs3087243 (PPA=.99) mapped in an acinar-specific cCRE,

230   although the region around the variant was also broadly accessible in regulatory T cells, in line

231   with the specialized function of *CTLA4* in regulatory T cells[54] (**Supplementary Figure 7d**).

232   Exocrine cCREs harboring T1D risk variants at these loci were also largely specific relative to

233   previous studies of accessible chromatin from stimulated immune cells[55] and cytokine-stimulated

234   islets[56] except for *CTLA4* which mapped in a stimulated immune site (**Supplemental Table 8**).

Risk variant at novel T1D locus has pancreatic ductal cell-specific effects on *CFTR*

236   As another example of an exocrine-specific T1D signal, at the *CFTR* locus fine-mapped variant

237   rs7795896 (PPA=0.60) mapped in a distal cCRE highly specific to pancreatic ductal cells

238   upstream of the *CFTR* gene (**Figure 4a**). Furthermore, the cCRE harboring rs7795896 had ductal

239   cell-specific co-accessibility with the *CFTR* promoter in addition to several other genes (**Figure**

240   **4a**). Recessive mutations in *CFTR* cause cystic fibrosis (CF) which is often comorbid with exocrine

241   pancreas insufficiency and CF-related diabetes (CFRD)[57]. Furthermore, carriers of *CFTR*

242   mutations often develop chronic pancreatitis[58]. As *CFTR* has not been previously implicated in

243   T1D, we sought to validate the mechanism of this locus. First, we determined whether rs7795896

244   had allele-specific activity using luciferase reporter and gel shift assays in Capan-1 cells, an

245   established model of ductal cell function[59]. We observed both significantly reduced enhancer

246   activity (P=3.35×10^{-2}, **Figure 4b**) and reduced protein binding for the T1D risk allele (**Figure 4c**).

247   The variant mapped in a predicted sequence motif for the ductal cell-specific transcription factor

248 HNF1B (**Supplemental Table 6**) and overlapped a HNF1B ChIP-seq site previously identified in

249 ductal cell models (**Supplemental Figure 8**).

250 To determine whether the enhancer harboring rs7795896 regulated the expression of *CFTR* in

251 ductal cells, we used CRISPR interference (CRISPRi) to repress the activity of the enhancer

252 (*CFTR*[Enh]) in Capan-1 cells using two independent guide RNAs. As positive and negative controls,

253 we inactivated the *CFTR* promoter (*CFTR*[Prom]) and used a non-targeting guide RNA, respectively.

254 RNA-seq analysis revealed a significant reduction in *CFTR* expression after enhancer inactivation

255 (*CFTR*[Enh] $\log_2(FC)$=-0.40, P=2.41x10^{-3}), whereas expression of other genes co-accessible with

256 the enhancer was unchanged (**Figure 4d**), identifying *CFTR* as a target gene of this enhancer.

257 We next determined whether risk variants affected *CFTR* expression directly using pancreas

258 eQTL data from GTEx[60]. Out of 13 genes tested by GTEx for association with these variants, only

259 *CFTR* had evidence for an eQTL (P=4.31×10^{-4}), and this eQTL was statistically colocalized with

260 the T1D signal (PP$_{shared}$=91.4%) (**Figure 4e**). The T1D risk allele C was also associated with

261 decreased *CFTR* expression, consistent with effects on enhancer activity and TF binding. To

262 evaluate whether the *CFTR* eQTL signal in whole pancreas tissue was driven by ductal cells, we

263 used MuSiC[61] to estimate cell type proportions in each GTEx pancreas RNA-seq sample (**Figure**

264 **4f, Supplemental Figure 9**). We then re-calculated eQTL association including estimated cell

265 type proportion for each sample as an interaction term in the model, and only ductal cells had

266 significant association (P=2.37×10^{-4}) (**Figure 4g**).

267 As *CFTR* has been implicated in risk of pancreatic cancer[62] and pancreatitis[63], we finally asked

268 whether rs7795896 was significantly associated with these phenotypes in the UK biobank[64],

269 FinnGen, and other GWAS[28–31]. The T1D risk allele (C) was associated with increased risk of

270 pancreatitis (chronic pancreatitis OR=1.15, P=3.18×10^{-3}; acute pancreatitis OR=1.07, P=1.15×10^{-2}

271), pancreatic cancer (OR=1.10, P=7.85×10^{-2}), and other pancreatic diseases which includes

272 pancreatitis and pancreatic cysts (OR=1.13, P=4.72×10^{-5}) (**Figure 4h**). In contrast, rs7795896 did

273 not show evidence for association with other autoimmune diseases (all P>.05), supporting that it

274 likely does not affect intrinsic immune cell function. Together our findings support a model in which

275 non-coding variants regulating the activity of genes such as *CFTR* in the exocrine pancreas

276 contribute to risk of T1D as well as pancreatic disease (**Figure 4i**).

277

278 **DISCUSSION**

279 Population-based association studies of complex disease are a powerful tool for genetic discovery

280 and, when coupled with cell type-resolved epigenome maps, can help reveal the cellular origins

281 of disease. Our results represent the largest genome-wide study of T1D genetics to date, more
282 than doubling the set of known risk signals, and provide a comprehensive resource for
283 interrogating T1D risk mechanisms. Integration of these data with cell type-specific accessible
284 chromatin maps both confirmed the prominent role of CD4+ T cells and implicated additional cell
285 types in disease risk notably pancreatic acinar and ductal cells. T1D risk variants mapped to
286 genes with specialized function in acinar and ductal cells such as *CFTR, GP2* and *CEL,* none of
287 which have been previously implicated in T1D. Observational studies have reported exocrine
288 pancreas abnormalities in T1D at disease onset[65] as well as in autoantibody positive individuals[66]
289 and first-degree relatives of T1D[67], but it was unknown whether this was contributing causally to
290 disease[68,69]. Studies in zebrafish, mice and humans have demonstrated that reduced *CFTR* leads
291 to CFRD via intra-islet inflammation and immune infiltration rather than intrinsic defects of beta
292 cell function, and immune infiltration in the exocrine pancreas has been suggested to contribute
293 to T1D pathogenesis[70–72]. We therefore hypothesize a causal role for gene regulation in exocrine
294 cells in T1D, potentially mediated through immune infiltration and inflammation, which may
295 provide novel avenues for therapeutic discovery in T1D.

296

METHODS

Genotype quality control and imputation

299 We compiled individual-level genotype data and summary statistics of 18,803 T1D cases and
300 470,876 controls of European ancestry from public sources (**Supplementary Table 1**), where
301 T1D case cohorts were matched to population control cohorts based on genotyping array
302 (Affymetrix, Illumina Infinium, Illumina Omni, and Immunochip) and country of origin where
303 possible (US, British, and Ireland). For the GENIE-UK cohort, because we were unable to find a
304 matched country of origin control cohort, we used individuals of British ancestry (defined by
305 individuals within 1.5 interquartile range of CEU/GBR subpopulations on the first 4 PCs from PCA
306 with European 1000 Genomes Project samples) from the University of Michigan Health and
307 Retirement study (HRS). For non-UK Biobank cohorts, we first applied individual and variant
308 exclusion lists (where available) to remove low quality, duplicate, or non-European ancestry
309 samples and failed genotype calls for each cohort. For control cohorts, we also used phenotype
310 files (where available) to remove individuals with type 2 diabetes or autoimmune diseases.

311 We then applied a uniform processing pipeline and used PLINK[73] to remove variants based on (i)
312 low frequency (MAF<1%), (ii) missing genotypes (missing>5%), (iii) violation of Hardy-Weinberg
313 equilibrium (HWE $p<1\times10^{-5}$ in control cohorts and HWE $p<1\times10^{-10}$ in case cohorts), (iv) substantial

314   differences in allele frequency compared to the Haplotype Reference Consortium r1.1 reference
315   panel[74], and (v) allele ambiguity (AT/GC variants with MAF>40%). We further removed individuals
316   based on (i) missing genotypes (missing>5%), (ii) sex mismatch with phenotype records
317   (het$_{chrX}$>.2 for females and het$_{chrX}$<.8 for males), (iii) cryptic relatedness through identity-by-
318   descent (IBD>.2), and (iv) non-European ancestry through PCA with 1000 Genomes Project[75] (>3
319   interquartile range from 25th and 75th percentiles of European 1KGP samples on the first 4 PCs)
320   (**Supplementary Figure 1**). For the affected sib-pair (ASP) cohort genotyped on the Immunochip,
321   we retained only one T1D sample from each family selected at random. For the GRID case and
322   1958 Birth control cohorts genotyped on the Immunochip, a portion of the cases overlapped the
323   T1DGC or 1958 Birth cohorts genotyped on a genome-wide array. We thus used sample IDs from
324   the phenotype files to remove these samples from the GRID and 1958 Birth cohorts and verified
325   that no samples were duplicated between the Immunochip and genome-wide array datasets by
326   checking IBD values. We combined data for matched case and control cohorts based on
327   genotyping array and country of origin for imputation. We used the TOPMed Imputation Server[76,77]
328   to impute genotypes into the TOPMed r2 panel[7] and removed variants based on low imputation
329   quality (R^2<.3). Following imputation, we implemented post-imputation filters to remove variants
330   based on potential genotyping or imputation artifacts based on empirical R^2 (genotyped variants
331   with empirical R^2<.5 and all imputed variants in at least low LD (r^2>.3) with them).

332   For the UK Biobank cohort, we downloaded imputed genotype data from the UK Biobank v3
333   release which were imputed using a combination of the HRC and UK10K + 1000 Genomes
334   reference panels. We used phenotype data to remove individuals of non-European descent. We
335   then used a combination of ICD10 codes to define 1,458 T1D cases (T1D diagnosis and insulin
336   treatment within a year of diagnosis, no T2D diagnosis). We defined controls as 362,257
337   individuals without diabetes (no T1D, T2D, or gestational diabetes diagnosis) or other
338   autoimmune diseases (systemic lupus erythematosus, rheumatoid arthritis, juvenile arthritis,
339   Sjögren syndrome, alopecia areata, multiple sclerosis, autoimmune thyroiditis, vitiligo, celiac
340   disease, primary biliary cirrhosis, psoriasis, or ulcerative colitis). We removed variants with low
341   imputation quality (R^2<.3).

342   For the FinnGen cohort, we downloaded GWAS summary statistics for type 1 diabetes
343   (E4_DM1_STRICT) from FinnGen freeze 2. This phenotype definition excluded individuals with
344   type 2 diabetes from both cases and controls.

Association testing, meta-analysis, and detection of conditional signals

We tested low-frequency and common variants (MAF>.001%) for association to T1D with firth bias reduced logistic regression using EPACTS (https://genome.sph.umich.edu/wiki/EPACTS) for non-UK Biobank cohorts or SAIGE[64] for the UK Biobank, using genotype dosages adjusted for sex and the first four ancestry PCs. We then combined association results across matched cohorts through inverse-variance weighted meta-analysis. We used the liftOver utility to convert GRCh38/hg38 into GRCh37/hg19 coordinates for all cohorts except for the UK biobank. We removed variants that were unable to be converted, were duplicated after coordinate conversion, or were located on different chromosomes after conversion. In total, our association data contained summary statistics for 59,244,856 variants. To evaluate the extent to which genomic inflation was driven by the polygenic nature of T1D or population stratification, we used LD score regression to compare the LDSC intercept to lambda genomic control (GC). We observed an intercept of 1.08 (SE=.03) compared to a lambda GC of 1.21, suggesting that the majority of the observed inflation was driven by polygenicity rather than population stratification.

We used a threshold of $P<5\times10^{-8}$ to define genome-wide significance for primary signals, and we defined novel loci as those statistically independent ($r^2<.01$) from reported index variants from previous T1D association studies. For all cohorts except for FinnGen, we performed exact conditional analyses on lead index variants to identify conditionally independent signals and used a locus-wide threshold of $P<1\times10^{-5}$ to define significance. For genomic regions with multiple known signals within close proximity, we conditioned on index variants from both signals. We iterated through this process for each locus until there were no remaining significant signals at the locus-wide threshold.

Fine mapping of distinct association signals

We constructed LD-based genetic credible sets of variants for 141 signals at 89 known and novel loci excluding the MHC locus for complex LD structure and *ICOSLG*, for which we were unable to find imputed proxy variants in our dataset. For the main signals at known loci, we defined credible set variants by taking all variants in at least low LD ($r^2>.1$) with newly identified index variants within a 5 Mb window. For both novel and conditional signals, we used the most significant variant at the signal and the same credible set definition. We used effect size and standard error estimates to calculate approximate Bayes factors[9] (ABF) for each variant; at signals with multiple distinct association signals, we derived values from the corresponding conditional analysis. We then calculated the posterior probability of association (PPA) for each variant by dividing its ABF by the sum of ABF for all variants in the signal's credible set. To derive

378   99% credible sets for each signal, we sorted variants for each signal by descending PPA and

379   retained variants that added up to a cumulative PPA>0.99. To verify that variant coverage across

380   different imputation panels did not affect fine mapping, we calculated the effective sample size for

381   all credible set variants. There were only 9 credible set variants in total with <50% of the maximum

382   effective sample size, all of which had PPA<.01, and we did not further filter these variants.

383   **GWAS correlation analyses**

384   We used LD score regression (version 1.0.1) to estimate genome-wide genetic correlations

385   between T1D and immune diseases[25–31,41,42], other diseases[32–40,64,78,79], and non-disease traits[43–

386   50,80–88], using European subsets of GWAS where applicable. For acute pancreatitis, chronic

387   pancreatitis, and pancreatic cancer, we used inverse variance weighted meta-analysis to combine

388   SAIGE analysis results from the UK biobank[64] (PheCodes 577.1, 577.2, and 157) and FinnGen

389   (K11_ACUTPANC, K11_CHRONPANC, C3_PANCREAS_EXALLC). We used pre-computed

390   European 1000 Genomes LD scores to calculate correlation estimates (r_g) and standard errors.

391   We then corrected p-values for multiple tests using FDR correction, considering traits with FDR<.1

392   as significant. We also performed genetic correlation analyses using a version of the T1D meta-

393   analysis excluding the Immunochip cohorts and observed highly similar results.

394   **Generation of snATAC-seq libraries**

395   Combinatorial indexing single cell ATAC-seq (snATAC-seq/sci-ATAC-seq). snATAC-seq was

396   performed as described previously[89,90] with several modifications as described below. For the islet

397   samples, approximately 3,000 islet equivalents (IEQ, roughly 1,000 cells each) were resuspended

398   in 1 mL nuclei permeabilization buffer (10mM Tris-HCL (pH 7.5), 10mM NaCl, 3mM MgCl$_2$, 0.1%

399   Tween-20 (Sigma), 0.1% IGEPAL-CA630 (Sigma) and 0.01% Digitonin (Promega) in water) and

400   homogenized using 1mL glass dounce homogenizer with a tight-fitting pestle for 15 strokes.

401   Homogenized islets were incubated for 10 min at 4°C and filtered with 30 μm filter (CellTrics). For

402   the pancreas samples, frozen tissue was pulverized with a mortar and pestle while frozen and

403   immersed in liquid nitrogen. Approximately 22 mg of pulverized tissue was then transferred to an

404   Eppendorf tube and resuspended in 1 mL of cold permeabilization buffer for 10 minutes on a

405   rotator at 4°C. Permeabilized sample was filtered with a 30μm filter (CellTrics), and the filter was

406   washed with 300 μL of permeabilization buffer to increase nuclei recovery.

407   Once permeabilized and filtered, nuclei were pelleted with a swinging bucket centrifuge (500 x g,

408   5 min, 4°C; 5920R, Eppendorf) and resuspended in 500 μL high salt tagmentation buffer (36.3 mM

409   Tris-acetate (pH = 7.8), 72.6 mM potassium-acetate, 11 mM Mg-acetate, 17.6% DMF) and

410   counted using a hemocytometer. Concentration was adjusted to 4500 nuclei/9 μl, and 4,500 nuclei

411   were dispensed into each well of a 96-well plate. Glycerol was added to the leftover nuclei
412   suspension for a final concentration of 25 % and nuclei were stored at -80°C. For tagmentation,
413   1 µL barcoded Tn5 transposomes[90] were added using a BenchSmart™ 96 (Mettler Toledo),
414   mixed five times and incubated for 60 min at 37°C with shaking (500 rpm). To inhibit the Tn5
415   reaction, 10 µL of 40 mM EDTA were added to each well with a BenchSmart™ 96 (Mettler Toledo)
416   and the plate was incubated at 37°C for 15 min with shaking (500 rpm). Next, 20 µL 2 x sort buffer
417   (2 % BSA, 2 mM EDTA in PBS) were added using a BenchSmart™ 96 (Mettler Toledo). All wells
418   were combined into a FACS tube and stained with 3 µM Draq7 (Cell Signaling). Using a SH800
419   (Sony), 20 nuclei were sorted per well into eight 96-well plates (total of 768 wells) containing
420   10.5 µL EB (25 pmol primer i7, 25 pmol primer i5, 200 ng BSA (Sigma))[90]. Preparation of sort
421   plates and all downstream pipetting steps were performed on a Biomek i7 Automated Workstation
422   (Beckman Coulter). After addition of 1 µL 0.2% SDS, samples were incubated at 55 °C for 7 min
423   with shaking (500 rpm). We added 1 µL 12.5% Triton-X to each well to quench the SDS and
424   12.5 µL NEBNext High-Fidelity 2× PCR Master Mix (NEB). Samples were PCR-amplified (72 °C
425   5 min, 98 °C 30 s, (98 °C 10 s, 63 °C 30 s, 72 °C 60 s) × 12 cycles, held at 12 °C). After PCR, all
426   wells were combined. Libraries were purified according to the MinElute PCR Purification Kit
427   manual (Qiagen) using a vacuum manifold (QIAvac 24 plus, Qiagen) and size selection was
428   performed with SPRI Beads (Beckmann Coulter, 0.55x and 1.5x). Libraries were purified one
429   more time with SPRI Beads (Beckmann Coulter, 1.5x). Libraries were quantified using a Qubit
430   fluorimeter (Life technologies) and the nucleosomal pattern was verified using a TapeStation
431   (High Sensitivity D1000, Agilent). The library was sequenced on a HiSeq2500 sequencer
432   (Illumina) using custom sequencing primers, 25% spike-in library and following read lengths: 50
433   + 43 + 40 + 50 (Read1 + Index1 + Index2 + Read2).

434   Droplet-based 10X single cell ATAC-seq (scATAC-seq). 10X scATAC-seq protocol from 10x
435   Genomics was followed: Chromium SingleCell ATAC ReagentKits UserGuide (CG000209, Rev
436   A). Cryopreserved PBMC samples were thawed in 37°C water bath for 2 min and followed 'PBMC
437   thawing protocol' in the UserGuide. After thawing cells, the pellets were resuspended again in 1
438   mL chilled PBS (with 0.04% PBS) and filtered with 50 µm CellTrics (04-0042-2317, Sysmex). The
439   cells were centrifuged (300g, 5 min, 4°C) and permeabilized with 100 µl of chilled lysis buffer
440   (10 mM Tris-HCl pH 7.4, 10 mM NaCl, 3 mM MgCl2, 0.1% Tween-20, 0.1% IGEPAL-CA630,
441   0.01% digitonin and 1% BSA). The samples were incubated on ice for 3 min and resuspended
442   with 1mL chilled wash buffer (10 mM Tris-HCl pH 7.4, 10 mM NaCl, 3 mM MgCl2, 0.1% Tween-
443   20 and 1% BSA). After centrifugation (500g, 5 min, 4°C), the pellets were resuspended in 100 µL
444   of chilled Nuclei buffer (2000153, 10x Genomics). The nuclei concentration was adjusted between

445   3,000 to 7,000 per µl and 15,300 nuclei which targets 10,000 nuclei was used for the experiment.

446   For pancreas tissue (pulverized as described above), approximately 31.7 mg of pulverized tissue

447   was transferred to a LoBind tube (Eppendorf) and resuspended in 1 mL of cold permeabilization

448   buffer (10mM Tris-HCL (pH 7.5), 10mM NaCl, 3mM MgCl$_2$, 0.1% Tween-20 (Sigma), 0.1%

449   IGEPAL-CA630 (Sigma), 0.01% Digitonin (Promega) and 1% BSA (Proliant 7500804) in water)

450   for 10 min on a rotator at 4°C. Permeabilized nuclei were filtered with 30 µm filter (CellTrics).

451   Filtered nuclei were pelleted with a swinging bucket centrifuge (500 x g, 5 min, 4°C; 5920R,

452   Eppendorf) and resuspended in 1 mL Wash buffer (10mM Tris-HCL (pH 7.5), 10mM NaCl, 3mM

453   MgCl$_2$, 0.1% Tween-20, and 1% BSA (Proliant 7500804) in molecular biology-grade water). Nuclei

454   wash was repeated once. Next, washed nuclei were resuspended in 30 µL of 1X Nuclei Buffer

455   (10X Genomics). Nuclei were counted using a hemocytometer, and finally the nuclei

456   concentration was adjusted to 3,000 nuclei/µl. 15,360 nuclei were used as input for tagmentation.

457

458   Nuclei were diluted to 5 µl with 1X Nuclei buffer (10x Genomics) and, mixed with ATAC buffer

459   (10x Genomics) and ATAC enzyme (10x Genomics) for tagmentation (60 min, 37°C). Single cell

460   ATAC-seq libraries were generated using the (Chromium Chip E Single Cell ATAC kit (10x

461   Genomics, 1000086) and indexes (Chromium i7 Multiplex Kit N, Set A, 10x Genomics, 1000084)

462   following manufacturer instructions. Final libraries were quantified using a Qubit fluorimeter (Life

463   technologies) and the nucleosomal pattern was verified using a TapeStation (High Sensitivity

464   D1000, Agilent). Libraries were sequenced on a NextSeq 500 and HiSeq4000 sequencer

465   (Illumina) with following read lengths: 50 + 8 + 16 + 50 (Read1 + Index1 + Index2 + Read2).

466

467   **Single cell chromatin accessibility data processing**

468   Prior to read alignment, we used trim_galore (version 0.4.4) to remove adapter sequences from

469   reads using default parameters. We aligned reads to the hg19 reference genome using bwa

470   mem[91] (version 0.7.17; parameters: '-M -C') and removed low mapping quality (MAPQ<30),

471   secondary, unmapped, and mitochondrial reads using samtools[92]. To remove duplicate

472   sequences on a per-barcode level, we used the MarkDuplicates tool from picard (parameters:

473   'BARCODE_TAG'). For each tissue and snATAC-seq technology, we used log-transformed read

474   depth distributions from each experiment to determine a threshold separating real cell barcodes

475   from background noise. We used 500 total reads (passing all filters) as the cutoff for combinatorial

476   barcoding snATAC and between 2,300 and 4,000 total reads, as well as at least 0.3 fraction of

477   reads in peaks for 10x snATAC-seq experiments (**Supplemental Figure 5a**).

478

Single cell chromatin accessibility clustering

479

480 We identified snATAC-seq clusters using a previously described pipeline with a few modifications.

481 For each experiment, we first constructed a counts matrix consisting of read counts in 5 kb

482 windows for each cell. Using scanpy[93], we normalized cells to a uniform read depth and log-

483 transformed counts. We extracted highly variable (*hv*) windows (parameters: 'min_mean=.01,

484 min_disp=.25') and regressed out the total log-transformed read depth within *hv* windows (usable

485 counts). We then merged datasets from the same tissue and performed PCA to extract the top

486 50 PCs. We used Harmony[94] to correct the PCs for batch effects across experiments, using

487 categorical covariates such as donor-of-origin (all tissues), biological sex (PBMCs), and snATAC-

488 seq assay technology (pancreas). We used the corrected components to construct a 30 nearest

489 neighbor graph using the cosine metric, which we used for UMAP dimensionality reduction

490 (parameters: 'min_dist=.3') and clustering with the Leiden algorithm[95] (parameters:

491 'resolution=1.5').

492 Prior to combining cells across all tissues, we performed iterative clustering to identify and remove

493 cells with aberrant quality metrics. First, we identified and remove clusters of cells with lower

494 quality metrics (islets: 948, pancreas: 2,588, PBMCs: 5,268 cells removed total), including lower

495 usable counts or fraction of reads in peaks. Next, after removing the low-quality cells and

496 repeating the previous clustering steps, we sub-clustered the resulting main clusters at high

497 resolution (parameters: 'resolution=3.0') to identify sub-clusters containing potential doublets

498 (islets: 886, pancreas: 4,495, PBMCs: 5,844 cells removed total). We noted that these sub-

499 clusters tended to have higher average usable counts, promoter usage, and accessibility at more

500 than one marker gene promoter. After removing 20,029 low-quality or potential doublet cells, we

501 performed one final round of clustering using experiments from all tissues, including tissue-of-

502 origin as another covariate. We further removed 672 cells mapping to improbable cluster

503 assignments (islet or pancreatic cells in PBMC clusters or vice versa). After all filters, we ended

504 up with 131,554 cells mapping to 28 distinct clusters with consistent representation across

505 samples from the same tissue (**Supplemental Figure 5b**). We cataloged known marker genes

506 for each cell type and assessed gene accessibility (sum of read counts across each gene body)

507 to assign labels to each cluster.

508

Single cell chromatin accessibility analyses

509

510 We identified chromatin accessibility peaks with MACS2[96] by calling peaks on aggregated reads

511 from each cluster. In brief, we extracted reads from all cells within a given cluster, shifted reads

512 aligned to the positive strand by +4 bp and reads aligned to the negative strand by -5 bp, and

513   centered the reads. We then used MACS2 to call peaks (parameters: '--nomodel --keep-dup-all')

514   and removed peaks overlapping ENCODE blacklisted regions[97]. We then merged peaks from all

515   28 clusters with bedtools[98] to create a consistent set of 448,142 regulatory elements for

516   subsequent analyses.

517   To compare accessible chromatin profiles from snATAC-seq to those from bulk ATAC-seq on

518   FACS purified cell types, we reprocessed published ATAC-seq data from sorted pancreatic[99] and

519   unstimulated immune cells[55]. We created pseudobulk profiles from the snATAC-seq data for each

520   donor and cluster, retaining those that contained information from at least 50 cells. We then

521   extracted read counts in the 448,142 merged peaks for all sorted and pseudobulk profiles. We

522   used PCA to extract the top 20 principal components and used UMAP for dimensionality reduction

523   and visualization (parameters: 'min_dist=.5, n_neighbors=80').

524   To identify cluster-specific peaks, we used logistic regression models for each peak treating each

525   cell as an individual data point. For each model, we used cluster assignment and covariates such

526   as donor-of-origin and the log usable count as predictors and binary accessibility of the peak as

527   the outcome to calculate t-statistics (t-stats) for specificity. For a given cluster, we defined cluster-

528   specific peaks by taking the top 1000 peaks with the highest t-stats, after first filtering out peaks

529   which also had high t-stats for other clusters (peak t-stat>90th percentile of all t-stats for the given

530   cluster in more than 2 other clusters). We then used GREAT[12] to annotate peaks and summarize

531   linked genes in the form of gene ontology terms for the set of cluster-specific peaks as compared

532   to all merged peaks.

533   We estimated TF motif enrichment z-scores for each cell using chromVAR[13] (version 1.5.0) by

534   following the steps outlined in the user manual. First, we constructed a sparse binary matrix

535   encoding read overlap with merged peaks for each cell. For each merged peak, we estimated the

536   GC content bias based on the hg19 human reference genome to obtain a set of matched

537   background peaks. To ensure a motif enrichment value for each cell, we did not apply any

538   additional filters based on total reads or the fraction of reads in peaks. Next, using 580 TF motifs

539   within the JASPAR 2018 CORE vertebrate (non-redundant) set[14], we computed GC bias-

540   corrected enrichment z-scores (chromVAR deviation scores) for each cell. To extract highly

541   variable TF motifs, we computed the enrichment variability of each motif across all cells and used

542   the median as the cutoff. For each cluster, we then computed the average TF motif enrichment

543   z-score across all cells in the cluster.

544   We used Cicero[24] (version 1.3.3) to calculate co-accessibility scores between pairs of peaks for

545   each cluster. As in the single cell motif enrichment analysis, we started from a sparse binary

546   matrix. For each cluster, we only retained merged peaks that overlapped peaks from the cluster.

547   Within each cluster, we aggregated cells based on the 50 nearest neighbors and used cicero to

548   calculate co-accessibility scores, using a 1 Mb window size and a distance constraint of 500 kb.

549   We then defined promoters as ±500 bp from the TSS of protein coding transcripts to annotate co-

550   accessibility links between distal and promoter peaks.

551   **GWAS enrichment analyses**

552   We used LD score regression[100] to calculate genome-wide enrichment z-scores for 32 diseases

553   and traits including T1D. We obtained GWAS summary statistics for autoimmune and

554   inflammatory diseases (immune-related)[25–31,41,42], other diseases[32–40], and quantitative

555   endophenotypes[43–52], and where necessary, we filled in variant IDs and alleles. Using the

556   'munge_sumstats.py' script, we converted summary statistics to the standard format for LD score

557   regression. For each cluster, we used overlap with chromatin accessibility peaks as a binary

558   annotation for variants. We also created a background annotation using merged peaks across all

559   clusters. Then, we computed annotation-specific LD scores by following the instructions for

560   creating partitioned LD scores. We used stratified LD score regression[53] to estimate enrichment

561   coefficient z-scores for each annotation relative to the background, which we defined as merged

562   peaks across all clusters combined with the annotations in the baseline-LD model (version 2.2).

563   Based on the enrichment z-scores, we computed one-sided p-values to assess significance and

564   corrected for multiple tests using the Benjamini-Hochberg procedure[101]. We also calculated

565   GWAS enrichment z-scores for T1D using a version of the meta-analysis excluding the

566   Immunochip cohorts and observed highly similar enrichment results. We used fgwas to estimate

567   enrichment within cell type-specific cCREs using 2000 variants per window.

568   **Annotating cell type mechanisms of variants at fine mapped signals**

569   We first annotated fine mapped variants with PPA>1% using broad genomic annotations. We

570   defined "coding" as coding exons of protein coding genes, "promoter" as ±500 bp from the TSS

571   of protein coding transcripts, and "distal" as peaks in any cell type that did not overlap promoter

572   regions. We then assigned variants to each group without replacement, in the priority

573   coding>promoter>distal. To then further breakdown distal variants, we assigned clusters to cell

574   type groups (CD4 T cell: naïve CD4 T, activated CD4 T, regulatory T; CD8 T cell: naïve CD8 T,

575   activated CD8 T, pancreatic CD8 T; NK cell: adaptive and cytotoxic NK; B cell: naïve and memory

576   B; monocyte/ MΦ: classical and non-classical monocyte, pancreatic macrophage; dendritic:

577   conventional and plasmacytoid dendritic; other cell: megakaryocyte, endothelial, activated and

578   quiescent stellate; exocrine: acinar and ductal; endocrine: alpha, beta, delta, and gamma) and

579   created merged peak annotations for each group. We then assigned variants to each cell type

580   group without replacement, prioritizing groups in order based on their cumulative PPA.

581   **Luciferase reporter assay**

582   To test for allelic differences in enhancer activity at rs7795896, we cloned human DNA sequences

583   (Coriell) containing the reference or alternate allele upstream of the minimal promoter in the

584   luciferase reporter vector pGL4.23 (Promega) in the forward direction using the restriction

585   enzymes SacI and KpnI. We then created a construct containing the alternate allele using the

586   NEB Q5 SDM kit (New England Biolabs). The primer sequences used were:

587

588   Cloning FWD_P1 TAGCGGTACCTAATGGGAAATCATGCCAACC

589   Cloning FWD_P2 AATAGAGCTCATGTGTGTGTGCTGGGATGT

590

591   We grew Capan-1 cells (ATCC) to approximately 70% confluency in 6-well dishes according to

592   ATCC culture recommendations. We co-transfected cells with either the experimental or empty

593   vector and pRL-SV40. We then lysed cells 48 hours post transfection and assayed them using

594   the Dual-Luciferase Reporter System (Promega). We normalized Firefly activity to Renilla activity

595   and expressed normalized results as fold change compared to the luciferase activity of the empty

596   vector. We used a two-sided t-test to compare the luciferase activity between the two alleles.

597

598   **Electrophoretic mobility shift assay**

599   We ordered 5' biotinylated and unlabeled (cold) oligos with the reference and alternate alleles

600   from Integrated DNA Technologies. We annealed oligos with an equivalent volume of equimolar

601   complementary oligo in a binding buffer containing 10mM Tris pH 8.0, 50mM NaCl, and 1mM

602   EDTA at 95ºC for 5 minutes and cooled them gradually to room temperature before further use.

603

604   C oligo: (5' biotin)CAATTAGATGTAACTCATTAACATTAGAAAAA

605   T oligo: (5' biotin)CAATTAGATGTAACTTATTAACATTAGAAAAA

606

607   We carried out binding reactions using the LightShift Chemiluminescent EMSA kit (Thermo

608   Fisher) according to manufacturer's instructions with the following adjustments: 100 fmol of

609   biotinylated probe per reaction and 20 pmol of non-biotinylated "cold" probe in competition

610   reactions. We used approximately 16 ug of nuclear protein extract from Capan-1 cells purified

611   using NE-PER Nuclear and Cytoplasmic Extraction Reagents (Thermo Fisher) per binding

612   reaction.

613

614   **CRISPR inactivation of enhancer element**

615   We maintained HEK293T cells in DMEM containing 100 units/mL penicillin and 100 mg/mL

616   streptomycin sulfate supplemented with 10% fetal bovine serum (FBS). To generate CRISPRi

617   expression vectors, we designed guide RNA sequences to target the enhancer containing

618   rs7795896 or the *CFTR* promoter. These guides, as well as a non-targeting control, were placed

619   downstream of the human U6 promoter in the pLV hU6-sgRNA hUbC-dCas9-KRAB-T2a-Puro

620   backbone (Addgene, #71236). The guide RNA sequences were:

rs7795896 enhancer guide 1	GTAGTTGGCTTCCTCAGTAAG
rs7795896 enhancer guide 2	GAACAGTATGATTTACGTAA
CFTR promoter	GCGCCCGAGAGACCATGCAG
Non-targeting control	GTGACGTGCACCGCGGTGTG

621

622   We generated high-titer lentiviral supernatants by co-transfection of the resulting plasmid and

623   lentiviral packaging constructs into HEK293T cells. Specifically, we co-transfected CRISPRi

624   vectors with the pCMV-R8.74 (Addgene, #22036) and pMD2.G (Addgene, #12259) expression

625   plasmids into HEK293T cells using a 1mg/mL PEI solution (Polysciences). We collected lentiviral

626   supernatants at 48 hours and 72 hours after transfection and concentrated lentiviruses by

627   ultracentrifugation for 120 minutes at 19,500 rpm using a Beckman SW28 ultracentrifuge rotor at

628   4°C.

629   We obtained Capan-1 pancreatic ductal adenocarcinoma cell lines from ATCC and cultured them

630   using Iscove's Modified Dulbecco's Media with 20% fetal bovine serum, 100 units/mL penicillin,

631   and 100 mg/mL streptomycin sulfate. 24 hours prior to infection, we passaged cells into a 6-well

632   plate at a density of 650,000 cells per well. The following day, we added fresh media containing

633   5ug/mL polybrene and 5uL/mL concentrated CRISPRi lentivirus to each well. We incubated the

634   cells at 37ºC for 30 minutes and then spun them in a centrifuge for 1 hour at 30ºC at 950 × g. 6

635   hours later, we replaced viral media with fresh base culture media and left the cells to recover.

636   After 48 hours, we replaced media daily with the addition of 2ug/mL puromycin for a further 72

637 hours. We then harvested infected cells and isolated RNA using the RNeasy® Micro Kit (Qiagen)

638 according to the manufacturer instructions.

Differential analysis of CRISPR inactivation experiments

640 We used STAR (version 2.7.3a) to map reads to the hg19 genome using ENCODE standard

641 options (parameters: '--outFilterType BySJout --outFilterMultimapNmax 20 --alignSJoverhangMin

642 8 --alignSJDBoverhangMin 1 --outFilterMismatchNmax 999 --outFilterMismatchNoverReadLmax

643 0.04 --alignIntronMin 20 --alignIntronMax 1000000 --alignMatesGapMax 1000000'). We then

644 used featureCounts (version 1.6.4) to count the number of uniquely mapped reads mapping to

645 genes in GENCODE v19 (parameters: '-Q 30 -p -B -s 2 --ignoreDup'). We used DESeq2 to

646 evaluate differential mRNA expression between either the *CFTR* enhancer (pooled data from both

647 guides), or promoter inactivation versus the non-targeting guide.

Colocalization and deconvolution of the pancreas *CFTR* eQTL

649 We obtained GTEx consortium release v7[60] eQTL summary statistics for pancreas tissue from

650 220 samples and used effect size and standard error estimates to calculate Bayes factors[9] for

651 each variant. Where a T1D-associated variant had evidence for a pancreas eQTL, we considered

652 all variants in a 500kb window around the T1D GWAS index variant, and used the coloc[102]

653 package to calculate the probability that the variants driving T1D association and eQTL signals

654 were shared. We considered signals as colocalized based on the probability that they were shared

655 ($PP_{shared} > .9$).

656 We downloaded and re-processed a published pancreas single cell RNA-seq dataset[103] of 12 islet

657 donors. After re-processing and generating a counts matrix with the 10x Genomics cellranger

658 (version 3.0.0) pipeline, we first used scanpy[93] and filtered out 1) cells with <500 genes expressed,

659 2) cells with >20% mitochondrial reads, or 3) genes expressed in <3 cells. To ensure clustering

660 would not be affected by read depth, we normalized the total counts per cell to 10k and

661 subsequently log-normalized the resulting counts. We identified highly variable genes (hvgs)

662 based on mean expression and dispersion with (parameters: 'min_mean=.005, max_mean=6,

663 min_disp=.1'). We then extracted counts for hvgs and regressed out the total read count within

664 the hvgs. After dimensionality reduction with PCA, we used harmony[94] with default parameters to

665 correct for batch effects due to donor. We used the top 30 corrected PCs for graph-based

666 clustering with the leiden algorithm[95] (parameters: 'resolution=1.25') and visualization on reduced

667 dimensions with UMAP[104] (parameters: 'min_dist=.3'). To assign cell types to each cluster, we

668 used well-established marker genes from literature and labelled 18,279 cells.

669   We used MuSiC[61] to estimate the proportions of major pancreatic cell types (acinar, duct, stellate,

670   alpha, beta, delta, gamma) in each pancreas sample from the GTEx v7 release. As input, we

671   used raw count matrices of the islet scRNA-seq and GTEx v7 pancreas samples and cell type

672   labels from the analysis of the former dataset. For each cell type, we used the proportion as an

673   interaction term and constructed linear models of CFTR expression (TMM normalized) as a

674   function of the interaction between genotype dosage and cell type proportion, accounting for

675   covariates used by GTEx including sex, sequencing platform, 3 genotype PCs, and 28 inferred

676   PCs from the expression data. From the original 30 inferred PCs, we excluded inferred PCs 2 and

677   3 because they were highly correlated (Spearman's $\rho > .7$) with acinar cell proportion.

Phenotype associations at *CFTR* variant

679   We tested for association of the T1D index variant rs7795896 at *CFTR* to pancreatic and

680   autoimmune disease phenotypes. For acute pancreatitis, chronic pancreatitis, and pancreatic

681   cancer, we used inverse variance weighted meta-analysis to combine SAIGE analysis results

682   from the UK biobank[64] (PheCodes 577.1, 577.2, and 157) and FinnGen (K11_ACUTPANC,

683   K11_CHRONPANC, C3_PANCREAS_EXALLC). As mutations that cause cystic fibrosis (CF)

684   map to this locus, which are risk factors for pancreatitis and pancreatic cancer, we determined

685   the impact of the most common CF mutation F508del/rs199826652 on the association results for

686   rs7795896. For T1D, we tested for association of rs7795896 conditional on F508del/rs199826652

687   in all cohorts except for FinnGen and observed no evidence for a difference in T1D association.

688   For pancreatitis and pancreatic cancer, we identified F508del/rs199826652 carriers in UK

689   Biobank and repeated the association analysis for these phenotypes in UK biobank data after

690   removing these individuals and observed no evidence of a change in the effect of rs7795896.

691

CODE AVAILABILITY

693   Code used for processing snATAC-seq datasets and clustering cells is available at

694   https://github.com/kjgaulton/pipelines/tree/master/T1D_snATAC_pipeline.

695

DATA AVAILABILITY

697   Summary statistics and fine mapping credible sets for T1D GWAS will be available in the GWAS

698   catalog and in the T1D Knowledge Portal (http://t1d.hugeamp.org). Raw data files for snATAC-

699   seq will be deposited to GEO, and processed data files for snATAC-seq will be available through

700   the Diabetes Epigenome Atlas (https://www.diabetesepigenome.org/).

701

822

AUTHOR CONTRIBUTIONS

824   K.J.G and J.C. designed the study and wrote the manuscript. J.C. performed the genetic

825   association and single cell accessible chromatin analyses. R.G., M.O. and S.Huang performed

826   molecular experiments of enhancer and variant function. J.Y.H and M.M. generated single cell

827   accessible chromatin data. P.B. and K.K. contributed to data analysis. D.U.G and S.P. supervised

828   the generation of single cell accessible chromatin and contributed to data interpretation and

829   analyses. M.S. supervised experiments related to enhancer function and contributed to data

830   interpretation. S.Heller and A.K. contributed to interpretation of experimental data.

831

832   **FIGURE LEGENDS**

833   **Figure 1. Genome-wide association and fine mapping identifies novel signals for T1D risk.**

834   (a) Manhattan plot showing genome-wide T1D association p-values (-log10 transformed). Novel

835   loci are colored in red and labeled based on the nearest gene, and index variants have larger

836   radii and are circled. The dotted line indicates genome-wide significance (P=5×10^{-8}). (b) Locus

837   plots showing independent association signals at the known *BACH2* locus (left) and the novel

838   *BCL11A* locus (right). For conditional signals, the variants used for conditional analysis are

839   indicated under the title in parentheses. Variants are colored (known=blue, novel=red) based on

840   linkage disequilibrium (r^2) with the index variant for each signal. The dotted line indicates the

841   genome-wide significance threshold (P=5×10^{-8}) for the main signal and the locus wide

842   significance threshold (P=1×10^{-5}) for the conditional signals. (c) Breakdown of 141 independent

843   T1D risk signals after conditional fine-mapping analyses. Among these were 89 main signals at

844   59 known loci (excluding the MHC region) and 30 novel loci, and 52 conditional signals including

845   43 at known loci and 9 at novel loci. (d) Breakdown of the number of signals per locus (top),

846   number of 99% credible set variants per signal from fine mapping (middle), and the number of

847   variants with posterior probability of association >1% (bottom).

848   **Figure 2. Comprehensive reference map of 131,554 single cell chromatin accessibility**

849   **profiles from T1D-relevant tissues.** (a) Clustering of accessible chromatin profiles from 131,554

850   cells from single cell experiments of peripheral blood mononuclear cells, whole pancreas tissue,

851   and purified pancreatic islets. Cells are plotted on the first two UMAP components and colored

852   based on cluster assignment. Clusters are grouped into categories of cell types, and the number

853   of cells in each cluster are shown next to its corresponding label. (b) Dot plot (top) of relative gene

854   accessibility (chromatin accessibility reads across gene bodies, averages for each cluster and

855   scaled from 0-100 across columns/clusters) showing examples of marker genes used to identify

856   cluster labels. Circle sizes are scaled according to the relative gene accessibility value. Genome

857   browser tracks (bottom) showing aggregated chromatin accessibility profiles in a 50 kb window

858   around selected marker genes. (c) Relative peak accessibility for 25,436 cluster-specific peaks

859   across all 28 clusters (left), and enriched gene ontology terms with GREAT for peaks specific to

860   pancreatic macrophages, activated stellate, ductal, and acinar cells (right). (d) Single cell motif

861   enrichment z-scores for TFs showing specificity for cell lineage (SPI – myeloid and B cells, ETS

862   – T cells, FOXA – pancreatic), cell type (NR5A – acinar, HNF1 – ductal, EBF – B cells), and cell

863   state (POU2 – memory B, TCF7 – naïve CD4 T, RUNX – adaptive NK) . The sequence logo for

864   the enriched motif is displayed to the left of each UMAP plot. (e) Examples of cell type-specific

865   co-accessibility between the promoter of AQP1 and distal sites in ductal cells (left,

866   chr7:30,000,000-31,100,000, scale: 0-10 CPM) and the promoter of CEL and distal sites in acinar

867   cells (right, chr9:135,800,000-136,000,000, scale: 0-10 CPM).

868   **Figure 3. Cell type-specific enrichment and mechanisms of T1D risk variants.** (a) Relative

869   LD score regression enrichment z-scores (enrichment relative to background genomic

870   annotations including a merged set of all peaks) for autoimmune and inflammatory diseases (top),

871   other diseases (middle), and non-disease quantitative endophenotypes (bottom) for cCREs active

872   in pancreatic and blood cell types and states. ***FDR<.001 **FDR<.01 *FDR<.1. (b) T1D

873   enrichment within cell type-specific cCREs. Labeled clusters have a positive enrichment estimate.

874   Points represent log-transformed fgwas enrichment estimates and lines represent 95%

875   confidence intervals. (c) Breakdown of cumulative fine mapping probability (PPA) (left) and fine

876   mapped variants (right). Variants and their probabilities are assigned without replacement to

877   annotations from top to bottom. Variants are first broken down by genomic annotations (top), and

878   variants overlapping a distal peak are further broken down by cell type groups (bottom). CD4 T

879   cell: naïve CD4 T + activated CD4 + regulatory T; exocrine: acinar + ductal; endocrine: GCG^{high}

880   alpha + GCG^{low} alpha + INS^{high} beta + INS^{low} beta + SST^{high} delta + SST^{low} delta + gamma;

881   monocyte/MΦ: classical monocyte + non-classical monocyte + pancreatic macrophage; NK cell:

882   cytotoxic NK + adaptive NK; B cell: naïve B + memory B; CD8 T cell: naïve CD8 T + activated

883   CD8 T + pancreatic CD8 T; other cell: megakaryocytes + activated stellate + quiescent stellate +

884   endothelial; dendritic: conventional dendritic + plasmacytoid dendritic. (d) Signals with the highest

885   cumulative PPA for cell type groups with at least 2.5 cumulative PPA. (e) The *GP2* signal contains

886   3 variants (rs4238595, rs8060932, and rs8060932) in a distal peak upstream of the *GP2* promoter

887   (top, chr16:20,300,000-20,380,000). These variants are linked to *GP2* through co-accessibility in

888   acinar cells and account for the majority of the causal probability (cumulative PPA=.98) for the

889   signal (middle). Genome browser tracks (bottom) show that chromatin accessibility at both the

890   peak and the *GP2* promoter is highly specific to acinar cells. (f) The top variant at the

891   *CTRB1/2/BCAR1* signal rs72802342 (middle) overlaps a distal peak co-accessible with the

892   *CTRB2 and CTRB1* promoters in acinar cells (top: chr16:75,220,000-75,260,000, hg19). Genome

893   browser tracks (bottom, scale: 0-15) show that chromatin accessibility at the *CTRB1* and *CTRB2*

894   promoters are highly specific to acinar cells. Fine mapped variants are colored based on linkage

895   disequilibrium to the index variant. Variants contained in the 99% credible set are circled in black.

896   **Figure 4. Fine-mapped variant at the *CFTR* locus mediates T1D risk through distal**

897   **regulation of *CFTR* in pancreatic ductal cells.** (a) The *CFTR* locus contains a single fine-

898   mapped variant (rs7795896) in a distal cCRE linked to the promoter of *CFTR* and several other

899   genes through co-accessibility (top; region shown: chr7:116,490,000-117,860,000). The cCRE is

900   located approximately 33 kb upstream of the *CFTR* promoter. Zoomed-in view (chr7:117,040,000-

901   117,140,000, scale: 0-5 CPM) of fine mapped variants (middle) and genome browser tracks

902   (bottom) at this locus show that the cCRE is highly specific to ductal cells. (b) Luciferase reporter

903   assay in Capan-1 cells transfected with pGL4.23 minimal promoter plasmids containing

904   rs7795896 in the forward orientation. Relative luciferase units represent Firefly:Renilla ratios

905   normalized to control cells transfected with the empty vector. P-values are from a two-tailed

906   Student's t-test. (c) Electrophoretic mobility shift assay (EMSA) with nuclear extract from Capan-

907   1 cells using probes from both alleles of rs7795896. Bands with specific binding are labeled. (d)

908   CRISPR interference-mediated inactivation of the distal site containing rs7795896 (*CFTR*[iEnh]; 2

909   guide RNAs; 3 replicates; n=6 total) or the *CFTR* promoter (*CFTR*[iProm]; n=3 replicates) in CAPAN-

910   1 cells. Differential analysis of genes with promoters co-accessible with the peak show that CFTR

911   expression is significantly reduced in both *CFTR*[iProm] and *CFTR*[iEnh] cells. Data are shown as

912   transcripts per million (TPM). Error bars show 95% confidence interval and datapoints underlying

913   each boxplot are shown. (e) Bayesian colocalization showing that the T1D risk signal (top) and

914   *CFTR* pancreas eQTL from GTEx v7 (bottom) are likely driven by the same causal variant.

915   Variants are colored based on the linkage disequilibrium to the index variant. Variants in the 99%

916   credible set are circled in black. (f) Heatmap showing the average expression (normalized counts,

917   scaled from 0-1 across cell types) of marker genes of different pancreatic cell types from single

918   cell RNA-seq. *CFTR* expression is highly specific to ductal cells. (g) Deconvolution of the *CFTR*

919   pancreas eQTL using *in-silico* cell type proportion estimation and re-analyses of GTEx pancreas

920   data using interaction analyses shows that the eQTL signal only has a significant interaction with

921   ductal cell proportion. (h) Forest plot showing association of pancreatic disease traits in a meta-

922   analysis of UK Biobank and FinnGen data for rs7795896 compared to association of autoimmune

923   traits from large European GWAS. (i) Variants regulating genes with specialized function in the

924   exocrine pancreas influence risk of type 1 diabetes. At the *CFTR* locus, a variant reducing ductal

925   cell enhancer activity and *CFTR* expression increases risk of T1D and other pancreatic disease,

926   and we hypothesize that these effects are mediated through inflammation and immune infiltration

927   in the exocrine pancreas.

REFERENCES

1. Katsarou, A. *et al.* Type 1 diabetes mellitus. *Nat. Rev. Dis. Primer* **3**, 17016 (2017).

2. Onengut-Gumuscu, S. *et al.* Fine mapping of type 1 diabetes susceptibility loci and evidence for colocalization of causal variants with lymphoid gene enhancers. *Nat. Genet.* **47**, 381–386 (2015).

3. Barrett, J. C. *et al.* Genome-wide association study and meta-analysis find that over 40 loci affect risk of type 1 diabetes. *Nat. Genet.* **41**, 703–707 (2009).

4. Cooper, J. D. *et al.* Meta-analysis of genome-wide association study data identifies additional type 1 diabetes loci. *Nat. Genet.* **40**, 1399–1401 (2008).

5. Wellcome Trust Case Control Consortium. Genome-wide association study of 14,000 cases of seven common diseases and 3,000 shared controls. *Nature* **447**, 661–678 (2007).

6. Bradfield, J. P. *et al.* A Genome-Wide Meta-Analysis of Six Type 1 Diabetes Cohorts Identifies Multiple Associated Loci. *PLOS Genet.* **7**, e1002293 (2011).

7. Taliun, D. *et al.* Sequencing of 53,831 diverse genomes from the NHLBI TOPMed Program. *bioRxiv* 563866 (2019) doi:10.1101/563866.

8. Raeder, H. *et al.* Mutations in the CEL VNTR cause a syndrome of diabetes and pancreatic exocrine dysfunction. *Nat. Genet.* **38**, 54–62 (2006).

9. Wakefield, J. Bayes factors for genome-wide association studies: comparison with P-values. *Genet. Epidemiol.* **33**, 79–86 (2009).

10. Aylward, A., Chiou, J., Okino, M.-L., Kadakia, N. & Gaulton, K. J. Shared genetic risk contributes to type 1 and type 2 diabetes etiology. *Hum. Mol. Genet.* (2018) doi:10.1093/hmg/ddy314.

11. Chiou, J. *et al.* Single cell chromatin accessibility reveals pancreatic islet cell type- and state-specific regulatory programs of diabetes risk. *bioRxiv* 693671 (2019) doi:10.1101/693671.

953   12.   McLean, C. Y. *et al.* GREAT improves functional interpretation of cis-regulatory regions.

954   *Nat. Biotechnol.* **28**, 495–501 (2010).

955   13.   Schep, A. N., Wu, B., Buenrostro, J. D. & Greenleaf, W. J. chromVAR: inferring

956   transcription-factor-associated accessibility from single-cell epigenomic data. *Nat. Methods*

957   **14**, 975–978 (2017).

958   14.   Khan, A. *et al.* JASPAR 2018: update of the open-access database of transcription

959   factor binding profiles and its web framework. *Nucleic Acids Res.* **46**, D1284 (2018).

960   15.   Chen, H. *et al.* PU.1 (Spi-1) autoregulates its expression in myeloid cells. *Oncogene* **11**,

961   1549–1560 (1995).

962   16.   Kaestner, K. H. The FoxA factors in organogenesis and differentiation. *Curr. Opin.*

963   *Genet. Dev.* **20**, 527–532 (2010).

964   17.   Eyquem, S., Chemin, K., Fasseu, M. & Bories, J.-C. The Ets-1 transcription factor is

965   required for complete pre-T cell receptor function and allelic exclusion at the T cell receptor

966   beta locus. *Proc. Natl. Acad. Sci. U. S. A.* **101**, 15712–15717 (2004).

967   18.   Hale, M. A. *et al.* The nuclear hormone receptor family member NR5A2 controls aspects

968   of multipotent progenitor cell formation and acinar differentiation during pancreatic

969   organogenesis. *Dev. Camb. Engl.* **141**, 3123–3133 (2014).

970   19.   De Vas, M. G. *et al.* Hnf1b controls pancreas morphogenesis and the generation of

971   Ngn3+ endocrine progenitors. *Dev. Camb. Engl.* **142**, 871–882 (2015).

972   20.   O'Riordan, M. & Grosschedl, R. Coordinate regulation of B cell differentiation by the

973   transcription factors EBF and E2A. *Immunity* **11**, 21–31 (1999).

974   21.   Corcoran, L. M. & Karvelas, M. Oct-2 is required early in T cell-independent B cell

975   activation for G1 progression and for proliferation. *Immunity* **1**, 635–645 (1994).

976   22.   Issuree, P. D. *et al.* Stage-specific epigenetic regulation of CD4 expression by

977   coordinated enhancer elements during T cell development. *Nat. Commun.* **9**, 3594 (2018).

978   23.   Rapp, M. *et al.* Core-binding factor β and Runx transcription factors promote adaptive

979   natural killer cell responses. *Sci. Immunol.* **2**, (2017).

980   24.   Pliner, H. A. *et al.* Cicero Predicts cis-Regulatory DNA Interactions from Single-Cell

981   Chromatin Accessibility Data. *Mol. Cell* **71**, 858-871.e8 (2018).

982   25.   Ji, S.-G. *et al.* Genome-wide association study of primary sclerosing cholangitis identifies

983   new risk loci and quantifies the genetic relationship with inflammatory bowel disease. *Nat.*

984   *Genet.* **49**, 269–273 (2017).

985   26.   Bentham, J. *et al.* Genetic association analyses implicate aberrant regulation of innate

986   and adaptive immunity genes in the pathogenesis of systemic lupus erythematosus. *Nat.*

987   *Genet.* **47**, 1457–1464 (2015).

988   27.   Cordell, H. J. *et al.* International genome-wide meta-analysis identifies new primary

989   biliary cirrhosis risk loci and targetable pathogenic pathways. *Nat. Commun.* **6**, 8019 (2015).

990   28.   Okada, Y. *et al.* Genetics of rheumatoid arthritis contributes to biology and drug

991   discovery. *Nature* **506**, 376–381 (2014).

992   29.   de Lange, K. M. *et al.* Genome-wide association study implicates immune activation of

993   multiple integrin genes in inflammatory bowel disease. *Nat. Genet.* **49**, 256–261 (2017).

994   30.   Dubois, P. C. A. *et al.* Multiple common variants for celiac disease influencing immune

995   gene expression. *Nat. Genet.* **42**, 295–302 (2010).

996   31.   Jin, Y. *et al.* Genome-wide association studies of autoimmune vitiligo identify 23 new risk

997   loci and highlight key pathways and regulatory variants. *Nat. Genet.* **48**, 1418–1424 (2016).

998   32.   Jansen, I. E. *et al.* Genome-wide meta-analysis identifies new loci and functional

999   pathways influencing Alzheimer's disease risk. *Nat. Genet.* **51**, 404–413 (2019).

1000   33.   Mahajan, A. *et al.* Fine-mapping type 2 diabetes loci to single-variant resolution using

1001   high-density imputation and islet-specific epigenome maps. *Nat. Genet.* **50**, 1505–1513

1002   (2018).

1003   34.   Nelson, C. P. *et al.* Association analyses based on false discovery rate implicate new

1004   loci for coronary artery disease. *Nat. Genet.* **49**, 1385–1391 (2017).

1005   35.   Stahl, E. A. *et al.* Genome-wide association study identifies 30 loci associated with

1006   bipolar disorder. *Nat. Genet.* **51**, 793–803 (2019).

1007   36.   Wray, N. R. *et al.* Genome-wide association analyses identify 44 risk variants and refine

1008   the genetic architecture of major depression. *Nat. Genet.* **50**, 668–681 (2018).

1009   37.   Grove, J. *et al.* Identification of common genetic risk variants for autism spectrum

1010   disorder. *Nat. Genet.* **51**, 431–444 (2019).

1011   38.   Watson, H. J. *et al.* Genome-wide association study identifies eight risk loci and

1012   implicates metabo-psychiatric origins for anorexia nervosa. *Nat. Genet.* **51**, 1207–1214

1013   (2019).

1014   39.   Schizophrenia Working Group of the Psychiatric Genomics Consortium. Biological

1015   insights from 108 schizophrenia-associated genetic loci. *Nature* **511**, 421–427 (2014).

1016   40.   Wuttke, M. *et al.* A catalog of genetic loci associated with kidney function from analyses

1017   of a million individuals. *Nat. Genet.* **51**, 957–972 (2019).

1018   41.   López-Isac, E. *et al.* GWAS for systemic sclerosis identifies multiple risk loci and

1019   highlights fibrotic and vasculopathy pathways. *Nat. Commun.* **10**, 4955 (2019).

1020   42.   Paternoster, L. *et al.* Multi-ancestry genome-wide association study of 21,000 cases and

1021   95,000 controls identifies new risk loci for atopic dermatitis. *Nat. Genet.* **47**, 1449–1456

1022   (2015).

1023   43.   Yengo, L. *et al.* Meta-analysis of genome-wide association studies for height and body

1024   mass index in ∼700000 individuals of European ancestry. *Hum. Mol. Genet.* **27**, 3641–3649

1025   (2018).

1026   44.   Horikoshi, M. *et al.* Genome-wide associations for birth weight and correlations with

1027   adult disease. *Nature* **538**, 248–252 (2016).

1028   45.   Jiang, X. *et al.* Genome-wide association study in 79,366 European-ancestry individuals

1029   informs the genetic architecture of 25-hydroxyvitamin D levels. *Nat. Commun.* **9**, 260 (2018).

1030   46.   Manning, A. K. *et al.* A genome-wide approach accounting for body mass index identifies

1031   genetic variants influencing fasting glycemic traits and insulin resistance. *Nat. Genet.* **44**,

1032   659–669 (2012).

1033   47.   Wheeler, E. *et al.* Impact of common genetic determinants of Hemoglobin A1c on type 2

1034   diabetes risk and diagnosis in ancestrally diverse populations: A transethnic genome-wide

1035   meta-analysis. *PLoS Med.* **14**, e1002383 (2017).

1036   48.   Day, F. R. *et al.* Large-scale genomic analyses link reproductive aging to hypothalamic

1037   signaling, breast cancer susceptibility and BRCA1-mediated DNA repair. *Nat. Genet.* **47**,

1038   1294–1303 (2015).

1039   49.   Day, F. R. *et al.* Genomic analyses identify hundreds of variants associated with age at

1040   menarche and support a role for puberty timing in cancer risk. *Nat. Genet.* **49**, 834–841

1041   (2017).

1042   50.   Savage, J. E. *et al.* Genome-wide association meta-analysis in 269,867 individuals

1043   identifies new genetic and functional links to intelligence. *Nat. Genet.* **50**, 912–919 (2018).

1044   51.   Saxena, R. *et al.* Genetic variation in GIPR influences the glucose and insulin responses

1045   to an oral glucose challenge. *Nat. Genet.* **42**, 142–148 (2010).

1046   52.   Strawbridge, R. J. *et al.* Genome-wide association identifies nine common variants

1047   associated with fasting proinsulin levels and provides new insights into the pathophysiology

1048   of type 2 diabetes. *Diabetes* **60**, 2624–2634 (2011).

1049   53.   Finucane, H. K. *et al.* Partitioning heritability by functional annotation using genome-wide

1050   association summary statistics. *Nat. Genet.* **47**, 1228–1235 (2015).

1051   54.   Wing, K. *et al.* CTLA-4 control over Foxp3+ regulatory T cell function. *Science* **322**, 271–

1052   275 (2008).

1053   55.   Calderon, D. *et al.* Landscape of stimulation-responsive chromatin across diverse

1054   human immune cells. *Nat. Genet.* **51**, 1494–1505 (2019).

1055   56.   Ramos-Rodríguez, M. *et al.* The impact of proinflammatory cytokines on the β-cell

1056   regulatory landscape provides insights into the genetics of type 1 diabetes. *Nat. Genet.* **51**,

1057   1588–1595 (2019).

1058   57.   Gibson-Corley, K. N., Meyerholz, D. K. & Engelhardt, J. F. Pancreatic Pathophysiology

1059   in Cystic Fibrosis. *J. Pathol.* **238**, 311–320 (2016).

1060   58.   Sharer, N. *et al.* Mutations of the cystic fibrosis gene in patients with chronic pancreatitis.

1061   *N. Engl. J. Med.* **339**, 645–652 (1998).

1062   59.   Namkung, W. *et al.* Ca2+ activates cystic fibrosis transmembrane conductance

1063   regulator- and Cl- -dependent HCO3 transport in pancreatic duct cells. *J. Biol. Chem.* **278**,

1064   200–207 (2003).

1065   60.   GTEx Consortium *et al.* Genetic effects on gene expression across human tissues.

1066   *Nature* **550**, 204–213 (2017).

1067   61.   Wang, X., Park, J., Susztak, K., Zhang, N. R. & Li, M. Bulk tissue cell type deconvolution

1068   with multi-subject single-cell expression reference. *Nat. Commun.* **10**, 1–9 (2019).

1069   62.   McWilliams, R. R. *et al.* Cystic fibrosis transmembrane conductance regulator (CFTR)

1070   gene mutations and risk for pancreatic adenocarcinoma. *Cancer* **116**, 203–209 (2010).

1071   63.   Noone, P. G. *et al.* Cystic fibrosis gene mutations and pancreatitis risk: relation to

1072   epithelial ion transport and trypsin inhibitor gene mutations. *Gastroenterology* **121**, 1310–

1073   1319 (2001).

1074   64.   Zhou, W. *et al.* Efficiently controlling for case-control imbalance and sample relatedness

1075   in large-scale genetic association studies. *Nat. Genet.* **50**, 1335–1341 (2018).

1076   65.   Virostko, J. *et al.* Pancreas Volume Declines During the First Year After Diagnosis of

1077   Type 1 Diabetes and Exhibits Altered Diffusion at Disease Onset. *Diabetes Care* **42**, 248–
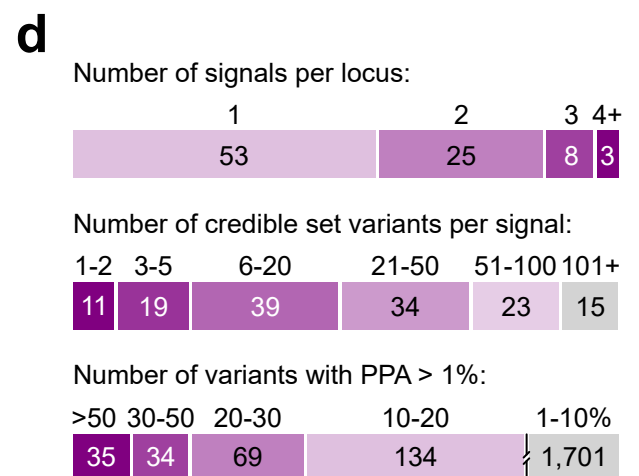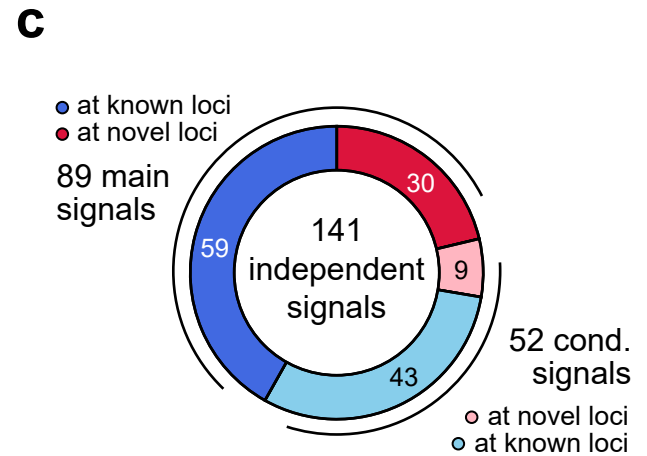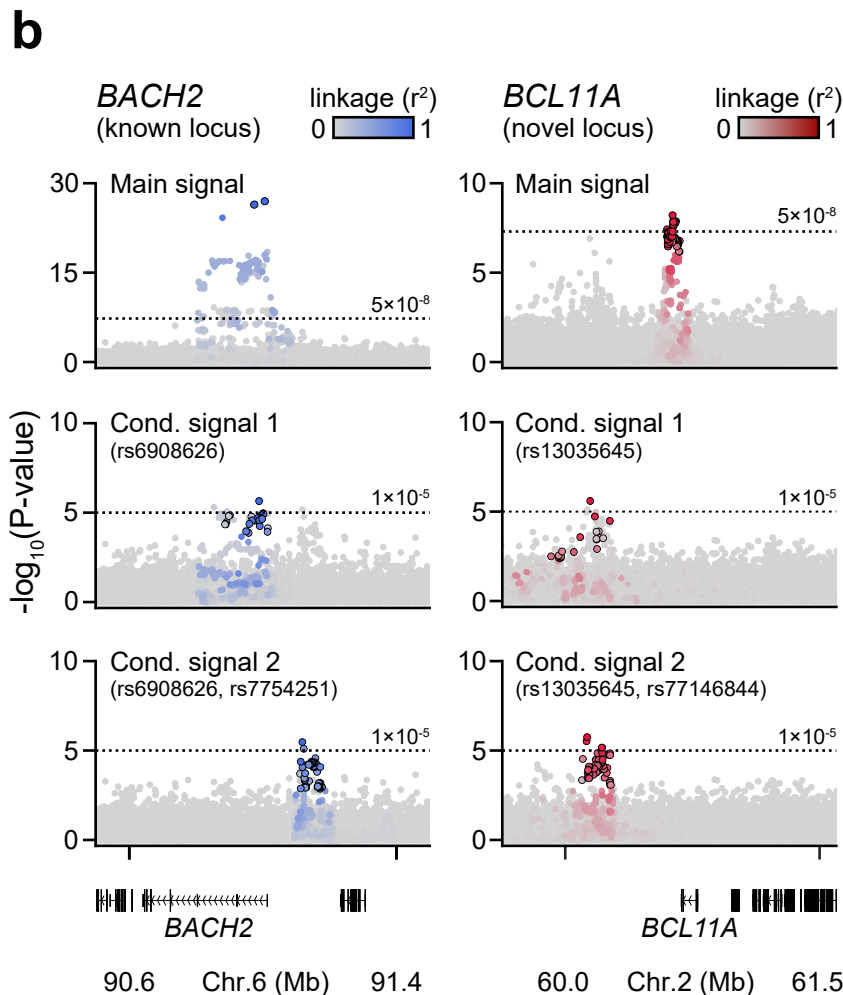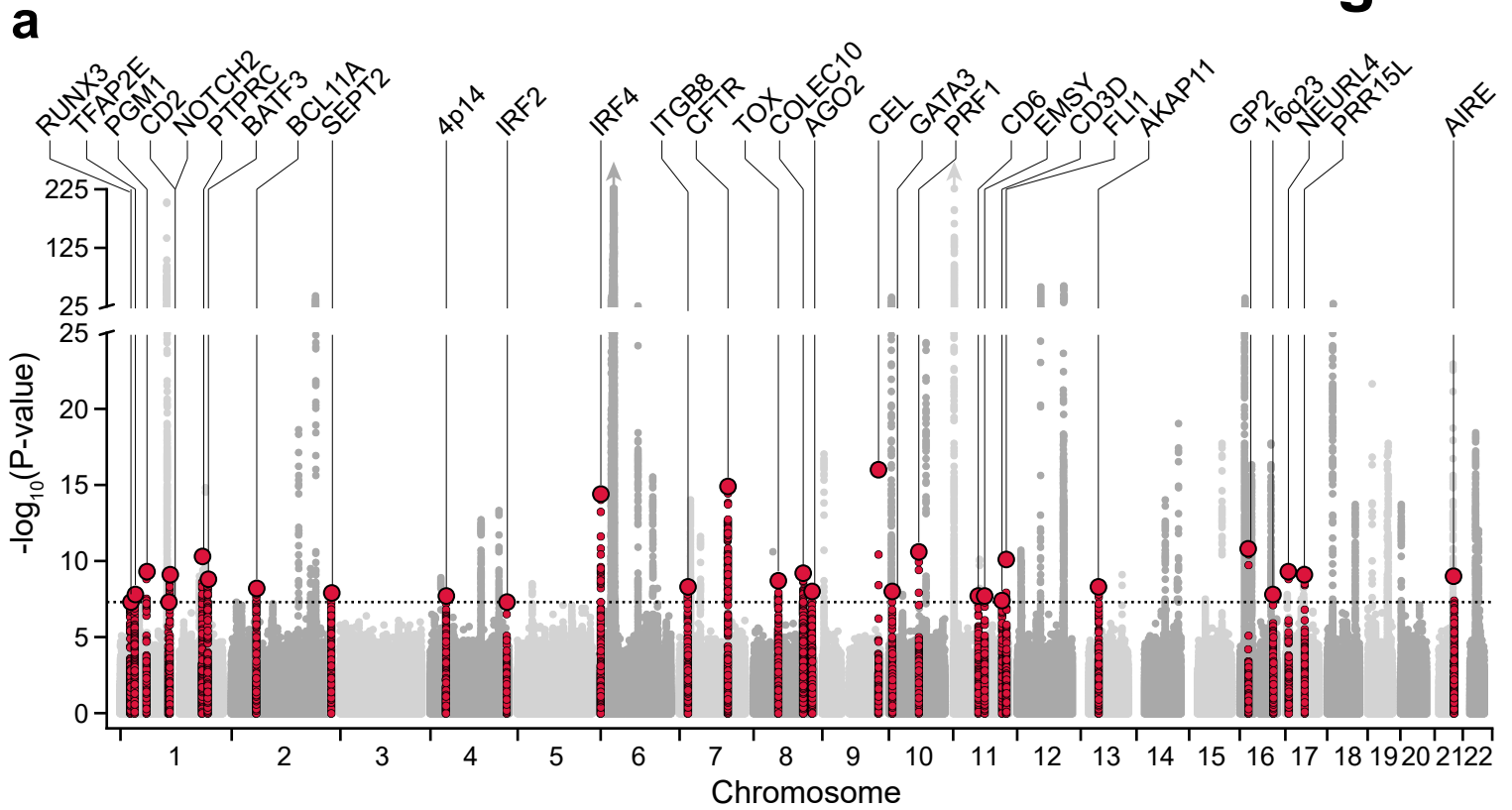
1078   257 (2019).

1079   66.   Campbell-Thompson, M., Wasserfall, C., Montgomery, E. L., Atkinson, M. A. & Kaddis,

1080   J. S. Pancreas organ weight in individuals with disease-associated autoantibodies at risk for

1081   type 1 diabetes. *JAMA* **308**, 2337–2339 (2012).

1082   67.   Campbell-Thompson, M. L. *et al.* Relative Pancreas Volume Is Reduced in First-Degree

1083   Relatives of Patients With Type 1 Diabetes. *Diabetes Care* **42**, 281–287 (2019).

1084   68.   Campbell-Thompson, M., Rodriguez-Calvo, T. & Battaglia, M. Abnormalities of the

1085   Exocrine Pancreas in Type 1 Diabetes. *Curr. Diab. Rep.* **15**, 79 (2015).

1086   69.   Campbell-Thompson, M. L. *et al.* The influence of type 1 diabetes on pancreatic weight.

1087   *Diabetologia* **59**, 217–221 (2016).

1088   70.   Hart, N. J. *et al.* Cystic fibrosis-related diabetes is caused by islet loss and inflammation.

1089   *JCI Insight* **3**, (2018).

1090   71.   Navis, A. & Bagnat, M. Loss of cftr function leads to pancreatic destruction in larval

1091   zebrafish. *Dev. Biol.* **399**, 237–248 (2015).

1092   72.   Valle, A. *et al.* Reduction of circulating neutrophils precedes and accompanies type 1

1093   diabetes. *Diabetes* **62**, 2072–2077 (2013).

1094   73.   Purcell, S. *et al.* PLINK: a tool set for whole-genome association and population-based

1095   linkage analyses. *Am. J. Hum. Genet.* **81**, 559–575 (2007).

1096   74.   McCarthy, S. *et al.* A reference panel of 64,976 haplotypes for genotype imputation. *Nat.*

1097   *Genet.* **48**, 1279–1283 (2016).

1098   75.   1000 Genomes Project Consortium *et al.* A global reference for human genetic variation.

1099   *Nature* **526**, 68–74 (2015).

1100   76.   Das, S. *et al.* Next-generation genotype imputation service and methods. *Nat. Genet.* **48**,

1101   1284–1287 (2016).

1102   77.   Fuchsberger, C., Abecasis, G. R. & Hinds, D. A. minimac2: faster genotype imputation.

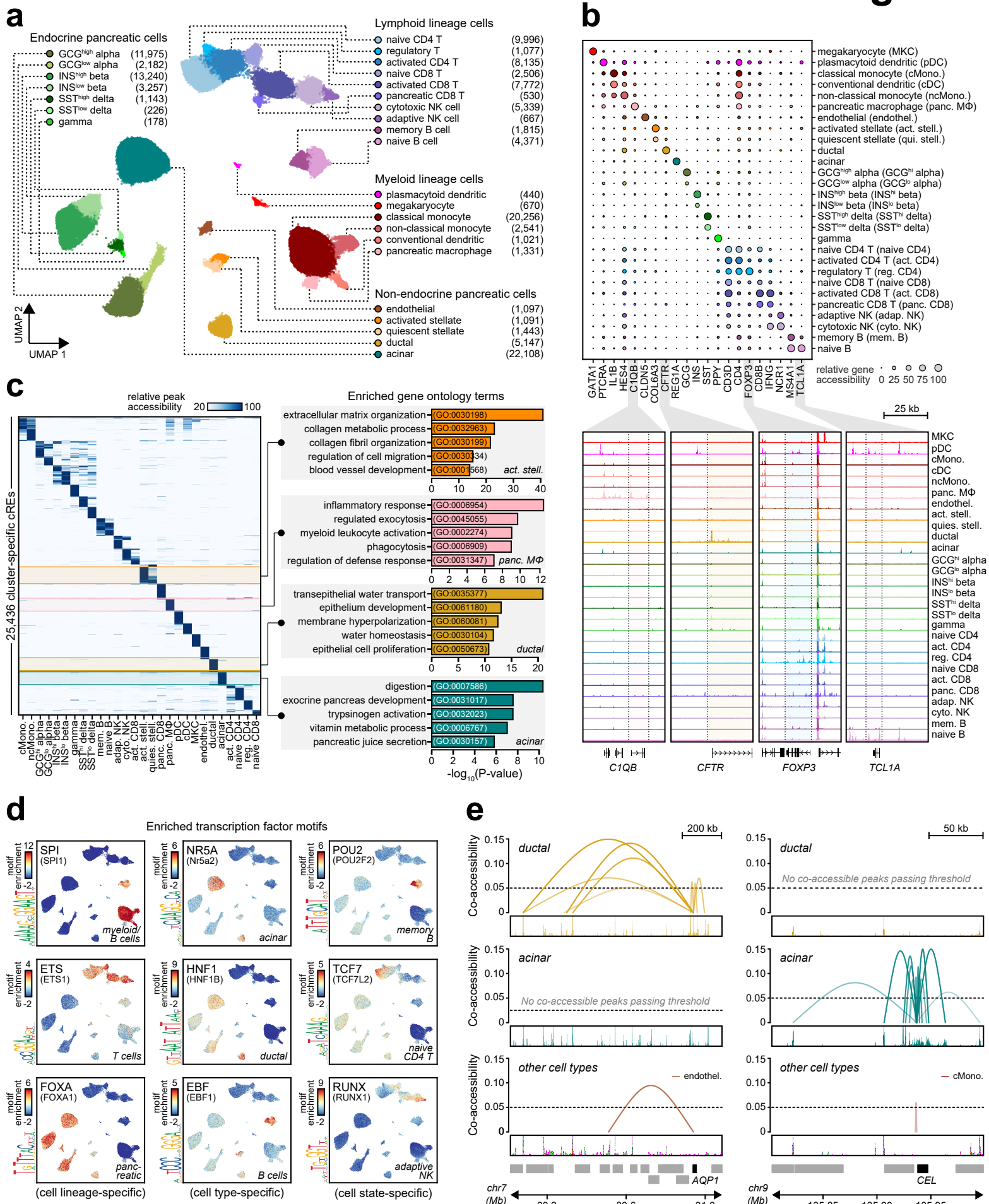1103   *Bioinforma. Oxf. Engl.* **31**, 782–784 (2015).

1104   78.   Nielsen, J. B. *et al.* Biobank-driven genomic discovery yields new insight into atrial

1105   fibrillation biology. *Nat. Genet.* **50**, 1234–1239 (2018).

1106   79.   Tachmazidou, I. *et al.* Identification of new therapeutic targets for osteoarthritis through

1107   genome-wide analyses of UK Biobank data. *Nat. Genet.* **51**, 230–236 (2019).

1108   80.   Taal, H. R. *et al.* Common variants at 12q15 and 12q24 are associated with infant head

1109   circumference. *Nat. Genet.* **44**, 532–538 (2012).

1110   81.   Teumer, A. *et al.* Genome-wide analyses identify a role for SLC17A4 and AADAT in

1111   thyroid hormone regulation. *Nat. Commun.* **9**, (2018).

1112   82.   Tobacco and Genetics Consortium. Genome-wide meta-analyses identify multiple loci

1113   associated with smoking behavior. *Nat. Genet.* **42**, 441–447 (2010).

1114   83.   Shungin, D. *et al.* New genetic loci link adipose and insulin biology to body fat

1115   distribution. *Nature* **518**, 187–196 (2015).

1116   84.   Jansen, P. R. *et al.* Genome-wide analysis of insomnia in 1,331,010 individuals identifies

1117   new risk loci and functional pathways. *Nat. Genet.* **51**, 394–403 (2019).

1118   85.   Cousminer, D. L. *et al.* Genome-wide association and longitudinal analyses reveal

1119   genetic loci linking pubertal height growth, pubertal timing and childhood adiposity. *Hum. Mol.*

1120   *Genet.* **22**, 2735–2747 (2013).

1121   86.   Felix, J. F. *et al.* Genome-wide association analysis identifies three new susceptibility

1122   loci for childhood body mass index. *Hum. Mol. Genet.* **25**, 389–403 (2016).

1123   87.   Willer, C. J. *et al.* Discovery and refinement of loci associated with lipid levels. *Nat.*

1124   *Genet.* **45**, 1274–1283 (2013).

1125   88.   van der Valk, R. J. P. *et al.* A novel common variant in DCST2 is associated with length

1126   in early life and height in adulthood. *Hum. Mol. Genet.* **24**, 1155–1168 (2015).

1127   89.   Cusanovich, D. A. *et al.* Multiplex Single Cell Profiling of Chromatin Accessibility by

1128   Combinatorial Cellular Indexing. *Science* **348**, 910–914 (2015).

1129   90.   Preissl, S. *et al.* Single-nucleus analysis of accessible chromatin in developing mouse

1130   forebrain reveals cell-type-specific transcriptional regulation. *Nat. Neurosci.* **21**, 432–439

1131   (2018).

1132   91.   Li, H. & Durbin, R. Fast and accurate long-read alignment with Burrows-Wheeler

1133   transform. *Bioinforma. Oxf. Engl.* **26**, 589–595 (2010).

1134   92.   Li, H. *et al.* The Sequence Alignment/Map format and SAMtools. *Bioinforma. Oxf. Engl.*

1135   **25**, 2078–2079 (2009).

1136   93.   Wolf, F. A., Angerer, P. & Theis, F. J. SCANPY: large-scale single-cell gene expression

1137   data analysis. *Genome Biol.* **19**, 15 (2018).

1138   94.   Korsunsky, I. *et al.* Fast, sensitive and accurate integration of single-cell data with

1139   Harmony. *Nat. Methods* **16**, 1289–1296 (2019).

1140   95.   Traag, V. A., Waltman, L. & van Eck, N. J. From Louvain to Leiden: guaranteeing well-

1141   connected communities. *Sci. Rep.* **9**, 1–12 (2019).

1142   96.   Zhang, Y. *et al.* Model-based analysis of ChIP-Seq (MACS). *Genome Biol.* **9**, R137

1143   (2008).

1144   97.   ENCODE Project Consortium. An integrated encyclopedia of DNA elements in the

1145   human genome. *Nature* **489**, 57–74 (2012).

1146   98.   Quinlan, A. R. & Hall, I. M. BEDTools: a flexible suite of utilities for comparing genomic

1147   features. *Bioinformatics* **26**, 841–842 (2010).

1148   99.   Arda, H. E. *et al.* A Chromatin Basis for Cell Lineage and Disease Risk in the Human

1149   Pancreas. *Cell Syst.* **7**, 310-322.e4 (2018).

1150   100.   Bulik-Sullivan, B. K. *et al.* LD Score regression distinguishes confounding from

1151   polygenicity in genome-wide association studies. *Nat. Genet.* **47**, 291–295 (2015).

1152   101.   Benjamini, Y. & Hochberg, Y. Controlling the False Discovery Rate: A Practical and

1153   Powerful Approach to Multiple Testing. *J. R. Stat. Soc. Ser. B Methodol.* **57**, 289–300 (1995).
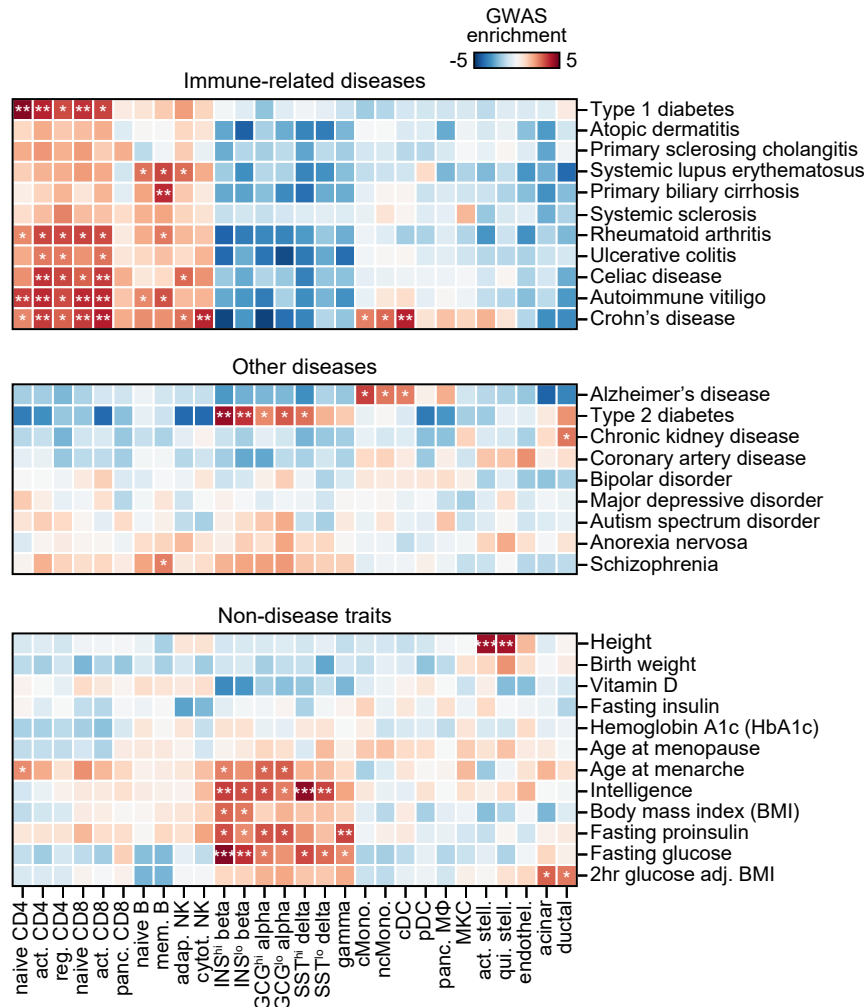
1154   102.   Giambartolomei, C. *et al.* Bayesian test for colocalisation between pairs of genetic

1155   association studies using summary statistics. *PLoS Genet.* **10**, e1004383 (2014).

1156   103.   Xin, Y. *et al.* Pseudotime Ordering of Single Human β-Cells Reveals States of Insulin

1157   Production and Unfolded Protein Response. *Diabetes* db180365 (2018) doi:10.2337/db18-

1158   0365.

1159   104.   McInnes, L. & Healy, J. UMAP: Uniform Manifold Approximation and Projection for

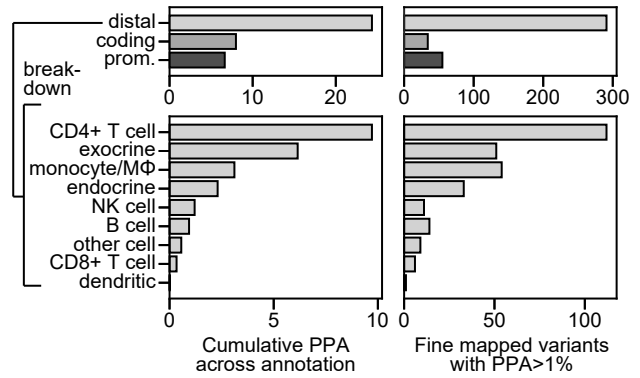1160   Dimension Reduction. *ArXiv180203426 Cs Stat* (2018).

1161
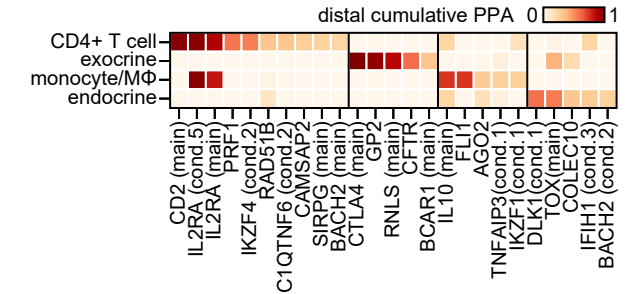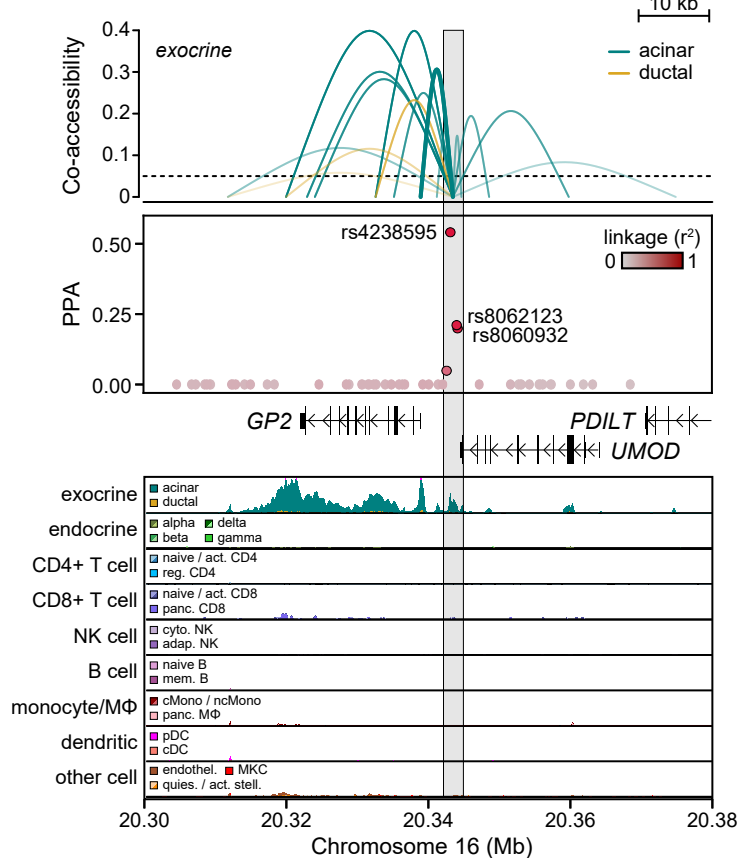
Figure 1

Figure 2

Figure 3

Figure 4